Journal of Structural Geology 158 (2022) 104582

Contents lists available at ScienceDirect

Journal of Structural Geology

journal homepage: www.elsevier.com/locate/jsg

Structural and temporal relationships between volcanic activity, hydrothermal alteration, epithermal Ag–Pb–Zn mineralization and regional stress regime in the Quevar Volcanic Complex (Puna plateau, Salta Province, NW Argentina)

Javier Escuder-Viruete [a,*], Eduardo A. Molina [b,c], Darío Chinchilla [d], Janet Gabites [e], Raúl Seggiaro [b], Cintia A. Marquetti [b], Nemesio Heredia [a]

[a] Instituto Geológico y Minero de España, CSIC, La Calera 1, Tres Cantos, 28760, Madrid, Spain
[b] Servicio Geológico y Minero Argentino, Av. B. Houssay 1099, B° Castañares, 4400, Salta, Argentina
[c] CONICET, Consejo Superior de Investigaciones Científicas y Técnicas. Universidad. Nacional de Salta, Av. Bolivia, 5150, Salta, Argentina
[d] Universidad Complutense de Madrid. Av. Séneca 2, Ciudad Universitaria, 28040, Madrid, Spain
[e] Pacific Centre for Isotopic and Geochemical Research, University of British Columbia, 6339 Stores Road, Vancouver, BC V6T-1Z4, Canada

ARTICLE INFO

Keywords:
Volcanism
Hydrothermal alteration
Epithermal mineralization
Geochronology
Fault-slip data inversion
Puna plateau

ABSTRACT

In the Cenozoic Central Volcanic Zone of the Andes, the genetic relationships between regional deformation, volcanic activity, and epithermal mineralization are not fully established. In order to shed some light on the matter, we present new macro and mesoscopic structural data, fault-slip data inversion and ^{40}Ar-^{39}Ar geochronology for volcanic rocks, hydrothermally altered equivalents and epithermal Ag–Pb–Zn mineralization of the Quevar Volcanic Complex, which is located in the Puna plateau of NE Argentina.

These data allow us to establish a first evolutionary stage with the eruption of the lavas and pyroclastic deposits of the Quevar Dacite in the Tortonian (9.9–8.7 Ma), when the volcanic activity was controlled by the NW-trending Calama-Olacapato-Toro lineament (COT). A second stage included the implantation of a hydrothermal alteration system and the related formation of the epithermal mineralization in the Messinian (7.7–6.3 Ma). These processes were contemporaneous with an ENE to E-directed shortening regime, which produced the reactivation of the COT and the formation of a left-lateral strike-slip stepover between WNW-trending regional faults. The third stage included the cessation of the hydrothermal activity and the erosion of the volcanic edifice. During this stage, mineralized veins and strike-slip faults were reactivated as normal faults by a NNW-directed extensional regime.

1. Introduction

Hydrothermal mineral deposits often occur spatially related to the geological structure (Hodgson, 1989). Well-established examples include mesothermal vein gold mineralization associated with ductile-brittle strike-slip shear zones (Robert et al., 2005; Micklethwaite et al., 2010; Wiemer et al., 2021), epithermal gold deposit hosted within brittle vein or dilatant fault networks at depths of less than 1 km (Simmons et al., 2005; Micklethwaite, 2009; Leary et al., 2016), and sediment-hosted (Carlin-type) gold mineralization associated with large-scale dip-slip faults (Hickey et al., 2014). Therefore, mineralizations associated with shear zones, veins and faults may be related to these pre-existing structural heterogeneities and/or to the processes that operated when these tectonic structures were active.

Shear zones, veins and faults associated to a fault system often exhibit systematic patterns in their geometry and scaling properties (Cowie et al., 1995; Bonnet et al., 2001; Davis, 2002). These systematic patterns are the cumulative result of multiple displacement events in the tectonic structure (Sibson, 2001), thus having implications in the formation and spatial location of mineral deposits in the upper crust (Boullier and Robert et al., 2005; Woodcock et al., 2007). Mineral deposits controlled by geological structures were often formed by

* Corresponding author. Instituto Geológico y Minero de España, C. La Calera 1, 28760, Tres Cantos, Madrid. Spain.
E-mail addresses: javier.escuder@csic.es (J. Escuder-Viruete), geoeduardomolina@gmail.com (E.A. Molina), dariochi@ucm.es (D. Chinchilla), jgabites@eoas.ubc.ca (J. Gabites), ruliseggiaro@yahoo.com.ar (R. Seggiaro), n.heredia@igme.es (C.A. Marquetti), cintia.marquetti@segemar.gov.ar (N. Heredia).

https://doi.org/10.1016/j.jsg.2022.104582
Received 17 October 2021; Received in revised form 15 March 2022; Accepted 28 March 2022
Available online 1 April 2022

processes with episodic behavior. Textures of multiple overprinting phases of brecciation and crack-seal in veins hosting ore are typical examples of this behavior as a "fault-valve" structure (Sibson, 1990, 1992, 2020; Cox, 2005). These textures can indicate dilatant faulting and repeated episodes of highly focused fluid flow along the structure due to overpressure (Peacock et al., 2017a), prior to the new cementation and sealing by precipitation of material transported in solution.

In the upper crust, typical geometric features of shear zones and faults are segmentation, multiple *en-échelon* segments, development of stepover zones (contractional and extensional), and braching at fault tips (Mann, 2007). Fault segmentation has been proposed to explain the spacing of mineral deposit clusters along structural systems (Robert et al., 2005; Micklethwaite et al., 2010). Mineralized faults and epithermal veins often comprise multiple segments that interact or link with adjacent segments across stepovers. Stepovers represent zones of more distributed strain, typically containing second-order structures such as branch faults, fracture networks and folds (Mann, 2007). Mineralization specifically is hosted in, or associated with, small displacement structures, some of which link across the stepover (Simmons et al., 2005).

Faults typically provide the pathways for fluids, volatile and metals to migrate upwards from magmatic-hydrothermal sources towards the surface (Sillitoe, 2010, 2015; Heinrich et al., 2004; Hedenquist and Taran, 2013). In this shallow crustal environment, a subsurface volumetrically significant alteration domain can be formed when ascending acidic magmatic-hydrothermal fluids react with wallrocks (Cooke et al., 2014). The resulting lithocap is characterized by development of a lithologically and/or structurally controlled zoned hydrothermal alteration, which provide criteria for epithermal mineralization exploration in conjunction to the geological structure (Hedenquist and Arribas, 2017).

In the Central Volcanic Zone of the Andes (18°–28° S), temporal and causal relationships between regional deformation, volcanic activity and related mineralization during Neogene are currently under discussion. The various alternatives proposed include: (1) variations in the regional stress-field that cause imbalance in a magmatic system close to the eruption (Sulpizio and Massaro 2017); (2) the (re)activation of crustal-scale N, NW and NE-striking fault zones that localize the volcanism (Riller et al., 2001; Trumbull et al., 2006; Guzmán et al., 2014; Tibaldi et al., 2017); (3) volcanic chains location related to the intersection between orogen-parallel N-striking structures and transversal NW-striking structures (Chernicoff et al., 2002; Richards et al., 2006; Trumbull et al., 2006; Seggiaro et al., 2019); and (4) the formation of large volcanic collapse calderas in relation to NW-trending lineaments, the NW-directed transtensive deformation or the transfer of movement between N-striking faults from the early Miocene (Petrinovic et al., 2010, 2017, 2021; Norini et al., 2013, 2014; Guzmán et al., 2017; de Silva and Kay, 2018; Seggiaro et al., 2021).

In order to shed some light on the matter, this paper present structural data at macroscopic and mesoscopic scales, fault-slip data inversion and ^{40}Ar-^{39}Ar geochronology data for volcanic rocks, hydrothermally altered lithological equivalents and associated epithermal Ag–Pb–Zn mineralization of the Quevar Volcanic Complex (QVC). The QVC is a large stratovolcano related to Neogene magmatism of the Central Andean Volcanic Zone, located in the Puna of the NW Argentina (Figs. 1 and 2; Kay et al., 1999; Quade et al., 2015; Petrinovic et al., 2017; Ramos, 2017). These data allow us to: (1) to determine the spatial and temporal relationships among felsic volcanism, hydrothermal alteration, epithermal Ag–Pb–Zn mineralization and diverse tectonic structures; (2) to establish the kinematics of faults measured in late Miocene volcanic rock; (3) to calculate the regional stress regime derived from the inversion of fault-slip data; and (4) to obtain the absolute age of the hosting volcanic rocks, the hydrothermal alteration and the associated epithermal mineralization. Finally, in conjunction with published regional data, we propose a structural evolutive model that integrates the volcanic, tectonic, hydrothermal alteration and mineralization processes in the QVC during the late Miocene.

2. Geological setting

2.1. The Altiplano-Puna plateau of the Central Andes

The geological domain of Altiplano-Puna is part of the Andean orogen, together with the Western Cordillera, the Eastern Cordillera, the Sub-Andean and the Sierras Pampeanas (Fig. 1). It constitutes a high elevation plateau (~4 km above sea level, average) located east of the Central Volcanic Zone segment of the Cenozoic Andean magmatic arc, which is related to the subduction of the Nazca Plate under the South American Plate (Allmendinger et al., 1997; Riller and Oncken, 2003; Ramos, 2009). The Puna is morphologically characterized by orogen-parallel N-trending mountain ranges cored by Neoproterozoic to Paleozoic rocks, separated by wide basins filled with Cenozoic volcanic and sedimentary rocks. In both the Puna and the Eastern Cordillera, the Lower Paleozoic and Cretaceous older structures controlled the Andean shortening, the architecture of the orogen and the evolution of the foreland basin during the Paleogene (Hongn et al., 2007; Norini et al., 2013; Quade et al., 2015; Montero-López et al., 2017; Seggiaro et al., 2017).

During the Cenozoic, the Altiplano-Puna plateau of the Central Andes was developed by the continuous subduction of the oceanic Nazca Plate in a convergent margin setting. In the South American upper plate, the E to ENE-directed convergence developed E and W-vergent thrusts-and-folds systems sub-parallel to the Andean mountain range. This horizontal shortening produced the crustal thickening and uplift of the Puna plateau and the Eastern Cordillera, and was coeval with the deposition of thick syntectonic strata (Allmendinger et al., 1989, 1997; Marrett et al., 1994; Elger et al., 2005; Oncken et al., 2006; Giambiagi et al., 2016).

2.2. Calama-Olacapato-El Toro lineament

The general N–S trend of the Andean folds and thrusts is locally rotated or interrupted by NW-trending structural lineaments (Fig. 1). Several authors relate the deflection in the trace of the regional Andean structures with the E to ENE-directed far stress field, which also produced the (re)activation and strike-slip motion on upper-crustal oblique fault zones or transfer zones, with displacements that can reach several tens of kilometers in the horizontal plane (Marrett et al., 1994; Riller and Oncken 2003; Acocella et al., 2011; Lanza et al., 2013; Seggiaro et al., 2019). These transverse structures have also controlled the distribution of late Cenozoic volcanism in the Central Andes, as well as the development of large volcanic collapse calderas (Riller et al., 2001; Ramelow et al., 2005; Richards et al., 2006; Guzmán et al., 2014, 2017; Tibaldi et al., 2017), with associated hot springs and polymetallic mineralizations.

In the northern Puna, the Calama-Olacapato-El Toro lineament (COT) controlled the building of a NW-trending volcanic chain in the upper Miocene, composed of the Rincón, Guanaquero, Chivinar, Tul-Tul, del Medio, Pocitos and Quevar stratovolcanoes (Fig. 2; Matteini et al., 2002; Acocella et al., 2011; Petrinovic et al., 2017). The origin of the transverse lineaments has been related to changes in the convergence angle between the Nazca and South America plates (Marrett et al., 1994), the orogen-parallel stretching (Riller and Oncken, 2003; Riller et al., 2001), or with transfer zones between thrust systems (Seggiaro and Hongn, 1999; Petrinovic et al., 2010; Norini et al., 2013; Acocella et al., 2011; Lanza et al., 2013; Seggiaro et al., 2016).

2.3. Neogene stress-field evolution in the Altiplano-Puna

The Altiplano-Puna crust has been deformed for the last time during the Andean orogeny from the early Oligocene to the late Miocene. Following the Eocene onset of shortening at the western protoplateau

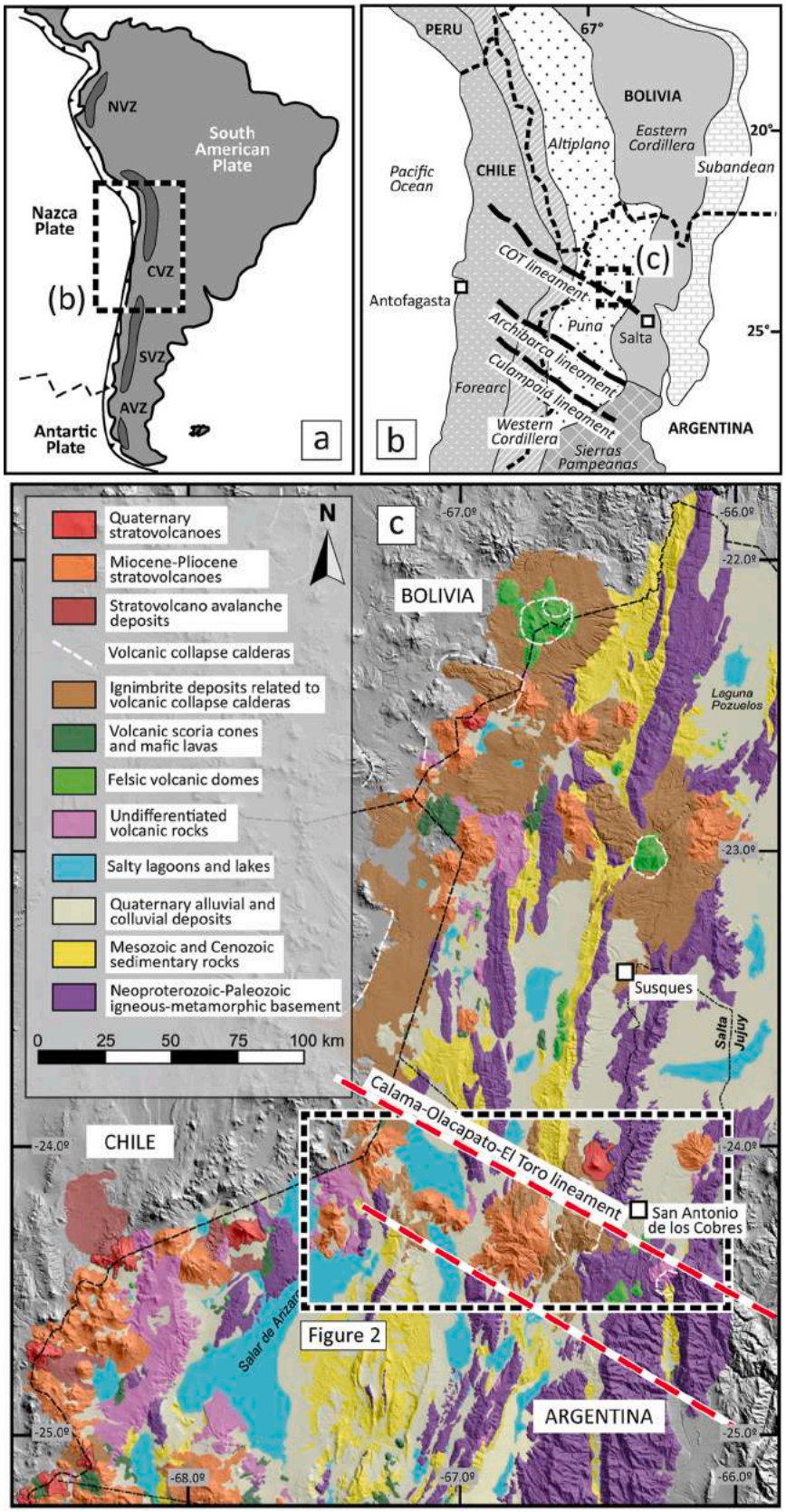

Fig. 1. (a) Northern, Central and Southern Volcanic Zones of the Andes. (b) Main characteristics and limits of the Morpotectonic Units of the Central Andes (Ramos, 2009, 2017). (c) Simplified geological map of the northern and central sectors of the Puna with emphasis on the location of stratovolcanoes, calderas and monogenetic volcanism (mod. of Petrinovic et al., 2017). Shaded relief in grayscale has been obtained from the GMRT data-set (Ryan et al., 2009) with *GeoMapApp* (www.geomapapp.org). The box marks the location of Fig. 2.

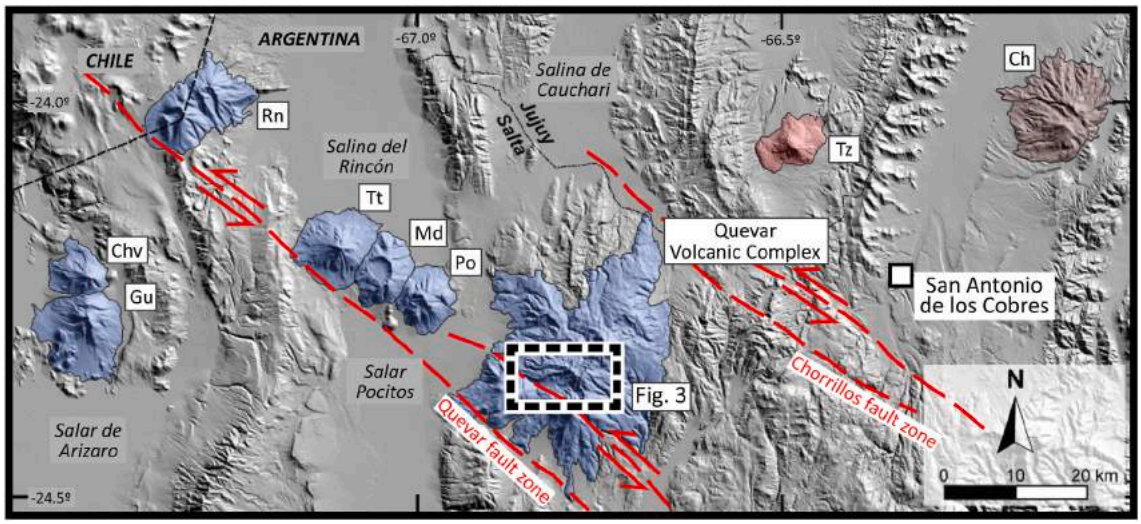

Fig. 2. Miocene-Pleistocene stratovolcanoes (in blue) and Quaternary (in red) related to the Calama-Olacapato-Toro lineament (Grosse et al., 2017; see regional situation in Fig. 1). Volcanoes: Ch; Chimpa, Rn; Rincon, Tz; Tuzgle, TT; Tul-Tul, Chv; Chivinar, Md; Del Medio, Po; Pocitos, Gu; Guanaquero, and Quevar Volcanic Complex (QVC). Shaded relief in grayscale has been obtained from the GMRT data-set (Ryan et al., 2009) with *GeoMapApp* (www.geomapapp.org). The box with the discontinuous black line marks the situation illustrated in Fig. 3.

margin, two main shortening peaks can be distinguished (e.g. Elger et al., 2005): early Oligocene (33-27 Ma) and middle/late Miocene (19-8 Ma). This early compressional stage dominated by E to ESE-directed horizontal shortening and lithospheric thickening was followed by a late Miocene to Recent stage characterized N to NNW-directed horizontal extension, which controlled the storage and eruption of caldera-related magmas (Allmendinger et al., 1989; Marrett et al., 1994; Cladouhos et al., 1994; Riller et al., 2001; Elger et al., 2005; Lanza et al., 2013; Daxberger and Riller, 2015). In the Western Cordillera, which represents the western margin of the Altiplano-Puna plateau, four stress regimes since the middle Miocene times have been described (Giambiagi et al., 2016): (1) an early to middle Miocene pure compression; (2) a late Miocene transpression; (3) a latest Miocene-early Pliocene phase characterized by partitioned normal and strike-slip faulting; and (4) a late Pliocene to Quaternary horizontal extension. The transition from a compressional to an extensional stress regime (*sensu* Peacock et al., 2017b) took place between 13-10 Ma and 8-5 Ma in the northern and southern Puna plateau, respectively. This change has been related to the increase in cortical thicknesses and regional topographic elevation to exceed threshold values in crustal strength, producing the orogenic collapse and the transfer of active shortening to the sub-Andean fold and thrust belt (Marrett et al., 1994; Cladouhos et al., 1994; Elger et al., 2005; Giambiagi et al., 2016).

2.4. Quevar Volcanic Complex

The Quevar Volcanic Complex covers an area of about 1,500 km^2 of the Salta Province in the Argentinean Puna. Outcrops of their volcanic rocks are generally located above 4,000 m, reaching altitudes between 5,810 m and 6,130 m above sea level (Fig. 2; Robl et al., 2009; Grosse et al., 2017; Petrinovic et al., 2017). The volume of volcanic materials emitted is estimated at 550 km^3, giving rise to one of the largest stratovolcanoes in the Puna.

2.4.1. Lithostratigraphic units

The QVC includes the effusive centers of Cerro El Quevar, Cerro Gordo and Cerro Azufre, which are aligned with the NW-trending COT (Fig. 2). The QVC is made from bottom to top by the following late Miocene lithostratigraphic Formations (Fig. 3; Robl, 2003): Tajamar Ignimbrite, Rhyolites and Perlites, Quevar Dacite, Rumibola Andesite and Cumbres Dacite.

The Tajamar Ignimbrite outcrops on the N and SE flanks of the QVC. It constitutes up to 400 m-thick accumulation of pyroclastic flows of riodacitic to dacitic composition and K-rich calc alkaline geochemical affinity, have a late Miocene age (10.3 ± 0.3 Ma; K–Ar whole-rock) and are genetically related to the Aguas Calientes caldera (Petrinovic et al., 2010, 2017, 2021). The Rhyolites and Perlites unit outcrops along the Quebradas Incahuasi and Quirón in the S and SW sectors of the QVC. It is made up of a devitrified rhyolitic extrusive dome, with brecciated and perlitic intrusive contacts. The Quevar Dacite constitutes the most extensive unit in the QVC and is made up of dacitic lavas and more subordinate pyroclastic deposits of block and ash flows emitted from various eruptive centers (Robl et al., 2009). In the Quebrada Incahuasi these deposits overlain the Rhyolites and Perlites unit. Typically, the dacites contain abundant phenocrysts of plagioclase and less abundant of pyroxene, hornblende, and biotite. Quartz phenocrysts are rare or absent. They include hornblende and plagioclase-rich mafic enclaves, suggesting a mixing of mafic and felsic magmas. The Rumibola Andesite unconformably overlain the Quevar Dacite. It includes the Azufre Andesite Member, which is composed of the andesitic lavas that outcrop at the Cerros Mamaturi and Quirón, as well as in the sector between the Cerros Azufre and Gordo. The Azufre Andesite thus records the transfer of volcanic activity to the SW sector of the QVC. The breccia and fumarolic sulfur deposits of Cerro Azufre define a semicircular structure related to a chimney of the volcano (Robl et al., 2009). The Esquina Azul Andesite Member integrates the andesitic-basaltic lavas emitted in the N sector of the QVC, which has provided an age of 8.3 ± 0.3 Ma (K–Ar whole-rock; Petrinovic et al., 2010). The Cumbres Dacite is formed by dacitic lavas rich in centimetric phenocrystals of sanidine, which cover the summits of Cerros Quevar and Gordo in the central sector of the QVC (Robl et al., 2009).

Overall, the QVC recorded a magmatic evolution from acidic to intermediate-basic compositional terms. The sequence began with the basal rhyolites of Quebradas Quirón and Incahuasi, continued with the main dacites of the central sector, and culminated with the andesites and basaltic andesites of the SW and N sectors. The final Cumbres Dacite departs from this compositional evolution.

2.4.2. Hydrothermal alteration

The QVC includes a pervasive lithocap located on the southwestern flank of the stratovolcano, along the Quebradas Incahuasi, Toro Grande and Mamaturi, where the hydrothermal alteration has an areal

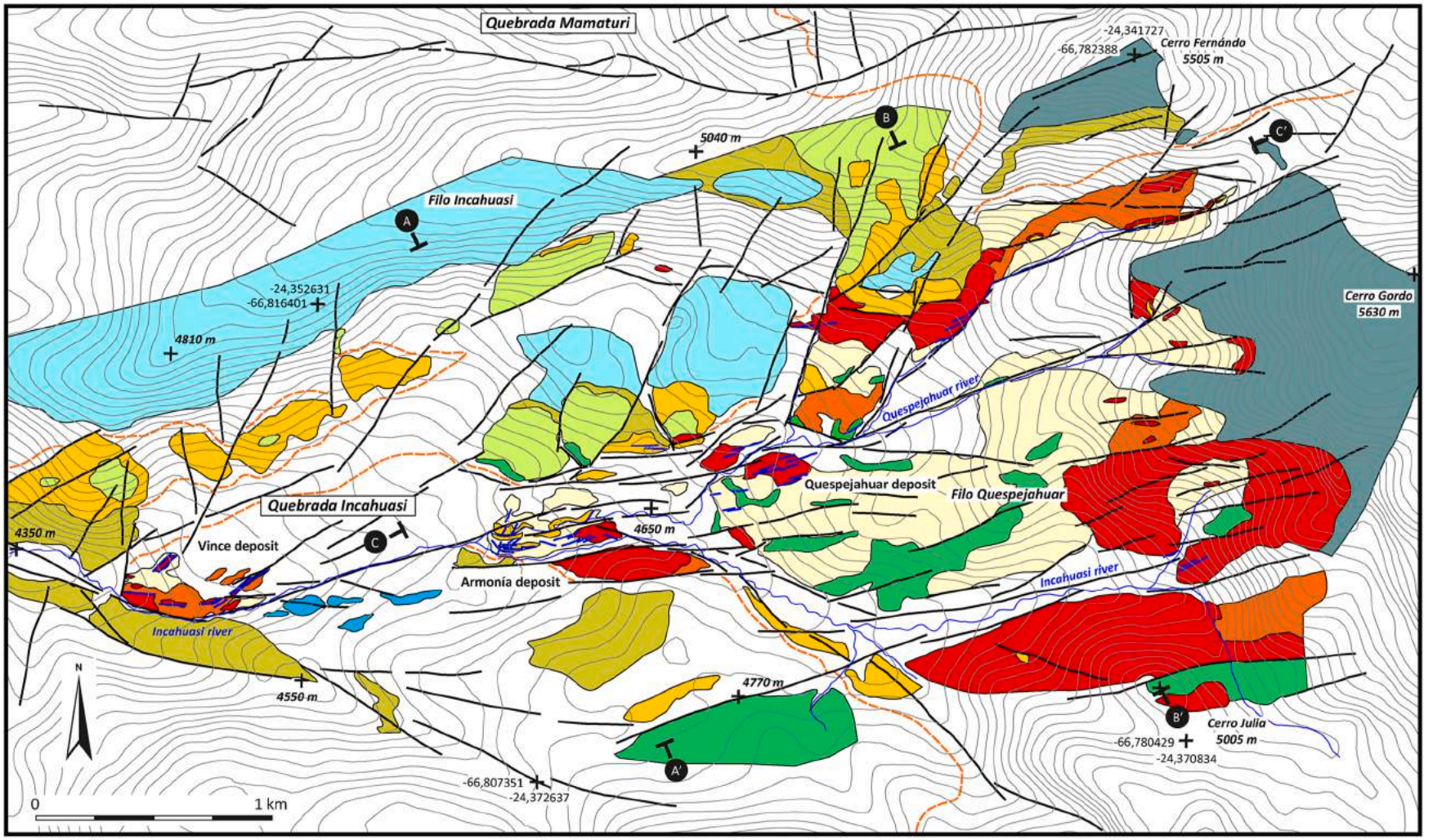

Fig. 3. Geologic map of the Quebrada Incahuasi of the Quevar Volcanic Complex (mod. Robl, 2003). Legend of lithostratigraphic units and hydrothermally altered equivalents are included in Fig. 4 and described in the text. Contour spacing is 20 m.

extension of about 50 km^2 and reaches a vertical thickness of 1.2 km (Robl et al., 2009; this work). Hydrothermal alteration affects the volcanic rocks of the Quevar Dacite, but it is not developed in the Azufre Andesite and in the Cumbres Dacite (Figs. 3 and 4). This alteration was apparently more intense in the volcaniclastic facies of breccia and tuff than in the coherent lavas. Following Cooke et al. (2014), it is possible to distinguish several mineralogical types of alteration in the Quebrada Incahuasi, which are briefly described below (see also Escuder-Viruete et al., 2021).

The dacites and andesites located near the summit of Cerro Fernando and to the S of the Vince deposit show a variable propylitic alteration. At the microscale, it is characterized by the partial or total pseudomorphic replacement of volcanic ferromagnesian minerals by secondary aggregates of chlorite, epidote and calcite, as well as plagioclase by calcite, epidote and zeolites. The volcanic groundmass has completely recrystallized to a very fine-grained aggregate composed of epidote, white mica, montmorillonite group minerals and zeolites. Between the zeolites, Robl et al. (2009) identify heulandite (stable at T < 210 °C), clinoptilolite, laumontite and yugawaralite. This mineral assemblage is typical of the epidote subzone of a low temperature propylitic alteration (e.g. Cooke et al., 2014), which is probably genetically related to the depth intrusion of a hydrous porphyry stock. Spatially associated with the propylitic alteration there is a replacement of the primary ferromagnesian minerals by pyrite, accompanied by the pseudomorphosis of feldspars and the groundmass by albite, quartz and zeolites.

The phyllic alteration is associated with the fault and breccia zones located eastern Filo Quespejahuar and southern Cerro Fernando, as well as the vicinity of the Armonía deposit. At the microscale, it is characterized by the replacement of plagioclase and the volcanic matrix by an aggregate of very fine-grained phyllosilicates.

The argillic, advanced argillic and silicic alterations present a great extension in the Quebrada Incahuasi, defining a broadly stratabound domain of approximately 1 km-thick and more than 3 km of visible lateral extension. These hydrothermal alterations caused the progressive loss of the volcanic mineralogy and textures. The transformation and leaching of the rock gave rise to its progressive whitening, highlighting in the landscape of the Quebrada Incahuasi (Fig. 4a). At the microscale and with an increasing degree of argillic alteration, the mineral association of montmorillonite, halloysite and illite is replaced by alunite, kaolinite, quartz, gypsum and sulfur. Alunite is especially abundant on the Filo Quespejahuar. Advanced argillic alteration is frequently accompanied by intense silicification. Leaching of volcanic phenocrysts and replacement of the groundmass by aggregates of very fine-grained quartz and/or amorphous silica results in vuggy-quartz textures. Both advanced argillic and silicic alterations overlap the propylitic alteration. Hypogene silicic, advanced argillic and argillic-altered rocks volumetrically define a lithocap in the sense of Cooke et al. (2014), which was formed by extensive water-rock interaction when acidic magmatic-hydrothermal fluids reacted with wallrock dacites during ascent towards the paleosurface (Sillitoe, 2010, 2015; Hedenquist and Taran, 2013). Therefore, it was probably formed above a shallow-crustal unexposed, hydrous intrusive complex.

In the Quebrada Incahuasi (Fig. 3), the lithocap is zoned and characterized by an outwards transition from a central silicic core composed of residual quartz (with massive and/or vuggy textures), through advanced argillic alteration (typically quartz-alunite) to argillic (quartz-kaolinite ± illite) and propylitic (chlorite-calcite ± epidote) assemblages (Escuder-Viruete et al., 2021). The fumarole sulfur deposits located at the highest topographic levels of Cerro Azufre and southward Cerro Fernando constitute the places of superficial discharge of the magmatic volatiles, probably located directly above the main upflow zone.

At elevations above 4500 m above sea level, precipitation/alteration products forming surficial insoluble minerals are widespread and related to a paleo-relief surface developed on top of Quevar Dacite. This supergenic alteration is characterized by the formation of iron oxides/hydroxides, clay minerals, manganese oxides and silica, which stains the rock in red-orange colors (Fig. 5g). At the microscale, it is made up of jarosite, goethite, hematite and limonite, among other minerals (Fig. 5h). The Rumibola Andesite and Cumbres Dacite unconformably overlie this leached cap.

2.4.3. Epithermal mineralization

In the Quebrada Incahuasi, the QVC contains a polymetallic epithermal system of Ag–Pb–Zn (Sb, As, Bi), which has been exploited mainly in the Vince, Armonía and Quespejahuar mineral deposits (Figs. 3 and 4). These deposits have been exploited intermittently, having provided about 3,000 tons of ore, with an average grade of 8.06% Pb and 0.26% Ag. Mineralization is located (Robl, 2003; Robl et al., 2009): (1) in vein systems and breccia cement; and (2) disseminated in pockets and more irregular domains of hydrothermaly altered rocks. The first type of deposit is mainly located along a ca. 3 km long, ENE-trending band (Fig. 3).

Robl et al. (2009) distinguish two main stages of mineralization. The first stage is made up of various mineral species of Ag in the Armonia deposit, which are members of the lillianite and andorite groups, as well as bournonite, galena and pyrite. The second stage consists mainly of galena and lead sulfosalts in barite gangue, among other mineral phases, which is present in all deposits. A third stage would be established in the minerals formed and metals remobilized during the supergenic alteration. Robl et al. (2009) indicate that mineralization is generally associated with vuggy-quartz, in the form of very fine-grained sulfides and sulfosalts, cementing the microbreccias of the host volcanic rock and filling the voids originated during the leaching of volcanic phenocrysts (Fig. 5e and f). The microtextural relationships between neotectonic structures and mineralization will be presented elsewhere.

3. Methodology

3.1. Mineralized veins and fault-slip data analysis

Stress or strain can be evaluated using inversion methods of brittle fault-slip data (Angelier, 1994). It involves collecting data of fault plane orientations, fault striae directions and sense of slip from kinematic indicators at the outcrop scale. Mesoscopic kinematic indicators used to infer the sense of slip on the fault-plane along the striae direction were the growth of fibrous crystals in steps, R and P-Riedel shears, grooves and crescent fractures, among others (e.g. Petit, 1987). In order to obtain from fault-slip data the principal stress axes ($\sigma_1 > \sigma_2 > \sigma_3$) and the stress ratio $R = (\sigma_2\text{-}\sigma_3/\sigma_1\text{-}\sigma_3)$ that best fit the reduced stress tensor at a given site, several inversion methods have been proposed (see reviews by Célérier et al., 2012; Sperner and Zweigel, 2010; Twiss and Unruh, 1998). Using multiple methods, hence different algorithms, will allow us to increase accuracy in the results by reducing the effect of systematic errors.

In natural conditions, fault-slip data sets measured at one location can be polyphasic, that is, include several fault subpopulations consistent with different stress tensors. The separation of the fault subpopulations referring to each tensor was performed prior to the inversion method for stress, calculating the pressure (P or compression axis) and tension (T or tensional axis) axes for each fault-slip data. Appearance of several clusters of P or T axes in stereographic projection were interpreted as indicative of the existence of fault-slip data related to different paleostress tensors, allowing their separation in fault subpopulations. Fault cross-cutting relationships, the overprinting of several striations in the same fault plane and the absolute age of the faulted rocks have also been used as criteria to date faults and thus paleostress tensors and tectonic phases.

Visualization of the fault-slip data in stereographic projection, statistical processing and inversion of the fault-slip data was performed with the *TectonicsFP* v1.7.9 software of Reiter and Acs (2000) and Ortner et al. (2002). Fault-slip data analysis and principal stress axes

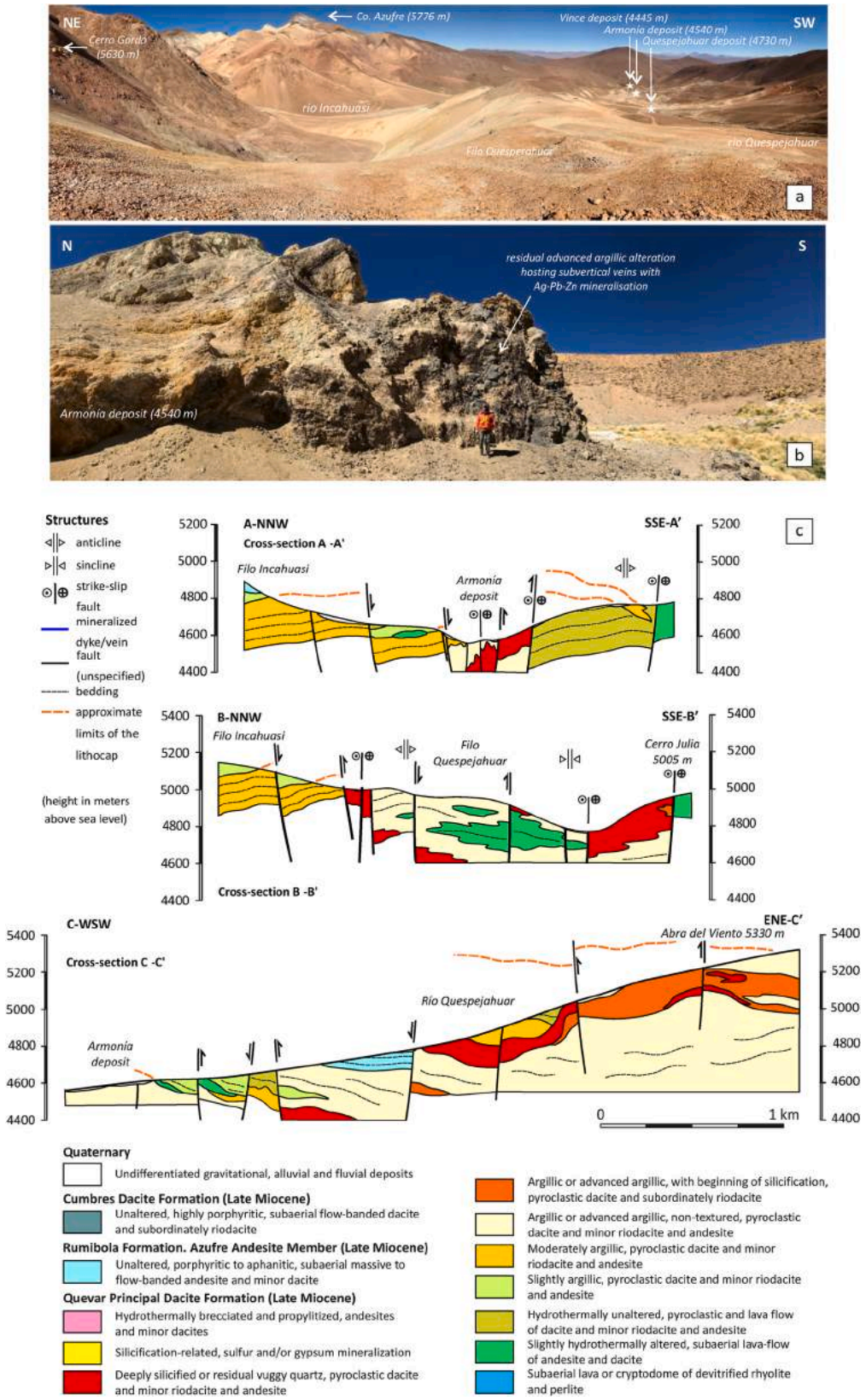

Fig. 4. (a) View at 5020 m above sea level showing the extent of the lithocap on the SW slope of Quebrada Incahuasi (rocks of white and yellow tones), where it constitutes an extensive domain of residual siliceous, advanced argillic and argillic hydrothermal alteration. This domain includes epithermal high-sulfidation Ag–Pb–Zn deposits in fault-hosted veins located along an ENE to E-trending corridor. (b) View of part of the Armonía deposit (4540 m; E.A. Molina serves as a scale) showing the topographically lower outcrop levels of the lithocap, where it is composed of an advanced argillic alteration containing sub-vertical veins with Ag–Pb–Zn mineralization. (c) Geological cross-sections through Quebrada Incahuasi showing their general tectonic architecture (locations in Fig. 3).

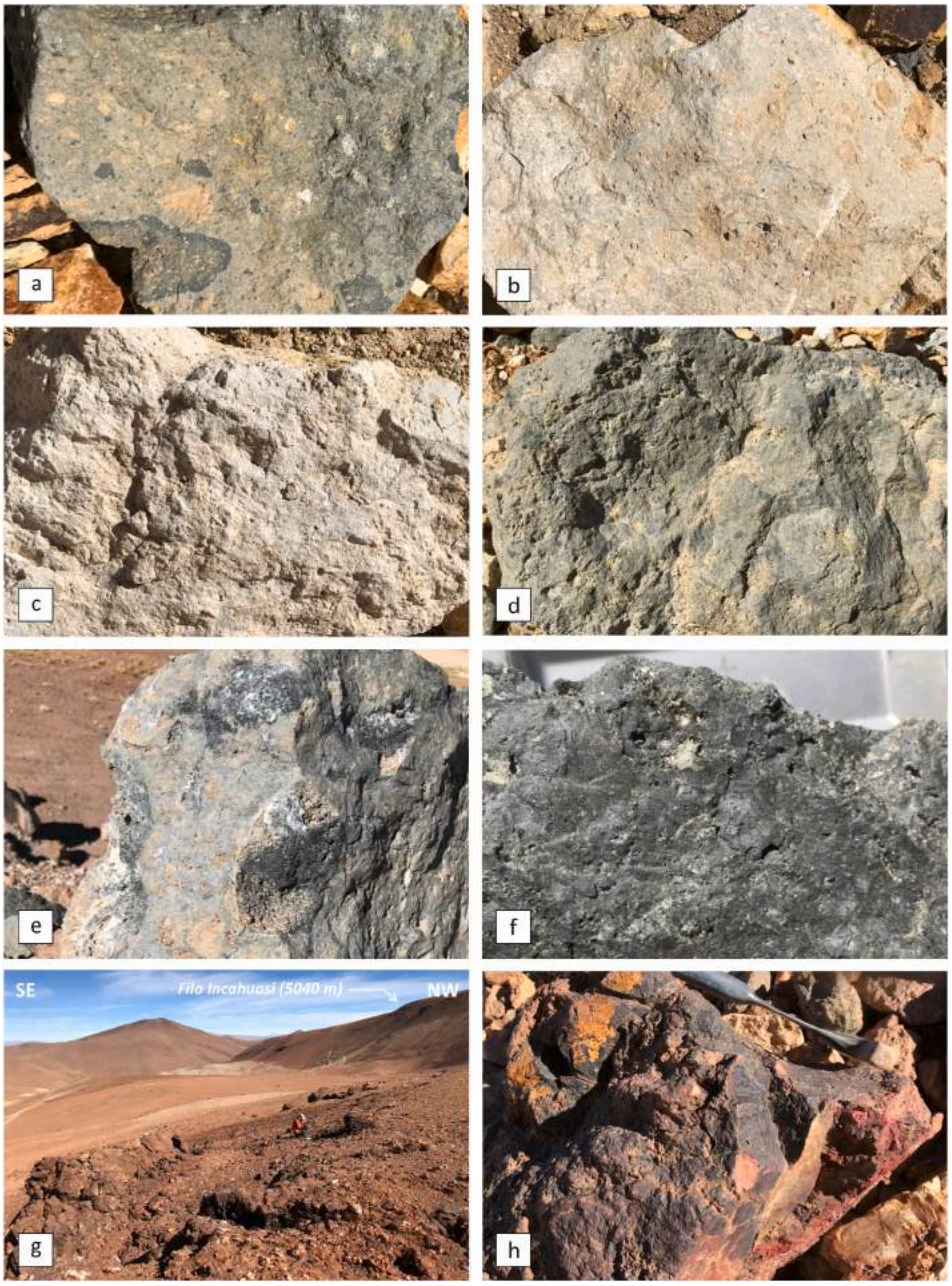

Fig. 5. Field photographs of volcanic rocks of the Quevar Dacite and hydrothermally altered equivalents. (a) Pyroclastic flow deposit composed of lithic fragments, crystals and juvenile clasts of scoria/pumice with ragged margins, product of an explosive magmatism (width of view 0.4 m). (b) Pyroclastic breccia preserving part of the primary texture affected by argillic to advanced argillic alteration (width of view 0.3 m). (c) Pyroclastic rock with advanced argillic alteration and total loss of volcanic texture (width of view 0.2 m). (d) Deeply silicified pyroclastic rock with residual quartz with massive and vuggy textures (width of view 0.4 m). (e) Deeply hydrothermally altered pyroclastic rock with mineralization of galena, sphalerite and pyrite in barite gangue, among other minerals (width of view 0.4 m). (f) Detail of massive sulphide (Pb–Zn–Sb) mineralization with barite filling voids (width of view 0.1 m). (g) Weathering of the upper part of the lithocap with replacement of sulfides by goethite, hematite and limonite, among other minerals, in the upper Quespejahuar valley. (h) Detail of the aggregate of jarosite, goethite, hematite and limonite produced by the supergenic alteration (width of view 0.2 m).

calculation were first performed with the kinematic right-dihedra method (Angelier, 1994), which shows the distribution of the percentage of compression or extension dihedra in stereographic projection. Inversion of fault-slip data was accomplished after with two inverse independent methods (Ortner et al., 2002, and references herein): direct inversion and numeric dynamic analysis. On the other hand, mineralized epithermal veins generally present a late brittle reactivation of their planes, which does not allow to obtain an unambiguous state of stress during their formation by means of kinematic analysis. In these conditions, clustering of vein data using a mixed Bingham distribution was used for paleostress analysis (Yamaji et al., 2010; Yamaji and Sato, 2011). Bingham distributions, or the orientation distributions with orthorhombic symmetry, has been applied to infer the state of stress during formation of magmatic dykes, mineral veins and fractures (Yamaji and Sato, 2011). In these works, the symmetry axes of the Bingham distribution of planar anisotropies (ε_1, ε_2 and ε_3 eigenvectors) correspond to the principal axes of the stress tensor (σ_1, σ_2 and σ_3, respectively). Yamaji et al. (2010) further argue that the stress ratio $R = (\sigma_2-\sigma_3)/(\sigma_1-\sigma_3)$ of the stress field related to the formation of an epithermal vein set could be approximated by the ratio of the concentration parameters κ_2/κ_1 of the Bingham distribution. Further explanation of the methodology of acquisition and analysis of mineralized veins and fault-slip data followed in this work is included in Appendix A of the electronic supplementary material.

3.2. $^{40}Ar/^{39}Ar$ geochronology analytical techniques

Rock samples for $^{40}Ar/^{39}Ar$ geochronology were crushed and sieved to obtain fragments ranging in the size range from 0.1 to 0.5 mm. The samples were rinsed in dilute nitric acid, washed in deionized water, rinsed and then air-dried at room temperature. Whole rock chips were stacked in an irradiation capsule with similar-aged samples and neutron flux monitors (Fish Canyon Tuff sanidine, 28.02 Ma; Renne et al., 1998). The samples were irradiated at the McMaster Nuclear Reactor in

Hamilton, Ontario, for 56 MWH, with a neutron flux of 3×10^{16} neutrons/cm^2. Analyses (n = 54) of 18 neutron flux monitor positions produced errors of <0.5% in the J value. The samples were step-heated at incrementally higher powers in the defocused beam of a 10 W CO_2 laser (New Wave Research MIR10) until fused, at the Noble Gas Laboratory of the Pacific Centre for Isotopic and Geochemical Research, University of British Columbia. The gas evolved from each step was analyzed by a VG5400 mass spectrometer equipped with an ion-counting electron multiplier. All measurements were corrected for total system blank, mass spectrometer sensitivity, mass discrimination, radioactive decay during and subsequent to irradiation, as well as interfering Ar from atmospheric contamination and the irradiation of Ca, Cl and K. Isotope production ratios were (^{40}Ar/^{39}Ar)K = 0.0302, (^{37}Ar/^{39}Ar)Ca = 1416.4306, (^{36}Ar/^{39}Ar)Ca = 0.3952, Ca/K = 1.83 (^{37}ArCa/^{39}ArK). The plateau and correlation ages were calculated using Isoplot 3.09 software (Ludwig, 2003). Errors are quoted at the 2σ (95% confidence) level and are propagated from all sources except mass spectrometer sensitivity and age of the flux monitor. The geologic time scale is from Cohen et al. (2013, updated in 2021).

4. Structure of the Quevar Volcanic Complex in the Quebrada Incahuasi

The structure of the QVC has been inferred from: (1) tectonic deformation affecting late Miocene volcanic rocks, hydrothermally altered equivalents and mineralization; (2) orientation of faults and folds at all scales; and (3) paleostress tensors and tectonic regimes deduced from the inversion of faults-slip data.

4.1. Field structural relationships

Our structural map compiled at the 1:10,000 scale covered the whole Quebrada Incahuasi and complements the work of Robl (2003). This fieldwork area was selected for its accessibility and for containing the main mineralized structures of the QVC. The geology of the Quebrada Incahuasi consists mainly of (Escuder-Viruete et al., 2021): (1) scarce remnants of a lower extrusive dome of rhyolites; (2) an intermediate group of faulted and folded dacites and subordinately andesites; (3) an upper unaltered sequence of slightly faulted and tilted andesites and dacites, that unconformably overlie an erosive surface developed on the intermediate volcanic rocks; and (4) an unconformable cover of Quaternary gravitational, alluvial and fluvial deposits. The spatial distribution of these groups of rocks is included in the lithological-structural map and cross-sections of Figs. 3 and 4. The lower rhyolitic dome and the variably altered intermediate dacites, as well as the hosting epithermal mineralization, are deformed by strike-slip and extensional faults. The upper sequence of andesites and dacites are deformed by normal or normal-oblique faults and were not affected by hydrothermal alteration.

Field mapping, microscopic observations and XRD whole-rock analysis have allowed to distinguish several lithological types in the intermediate Quevar Dacite, depending on the degree of the replacement of the volcanic mineralogy and textures by hydrothermal mineral assemblages in the lithocap (Figs. 3 and 4; Escuder-Viruete et al., 2021). In general, the coherent facies show slight alteration and are made up of porphyritic dacites and minor andesites characterized by a massive or flow foliated internal structure. They exhibit porphyritic and aphanitic textures produced by cooling and solidification of magma. These characteristics indicate that these are silicic subaerial lavas and extrusive domes, with associate autobreccias linked to the advance of the flows. The unaltered pyroclastic facies are little or no-vesicular and consist mainly of block and ash flow deposits of dacite and subordinately rhyodacite and andesite composition (Fig. 5a), resulting from explosive volcanic eruptions. These fragmentary facies are composed of poorly vesicular silicic juvenile clasts, crystals and sparse to abundant lithic fragments.

In the altered rocks and with the progressive increase of the hydrothermal replacement, lithological types are distinguished with a slight or non-existent argillic alteration, a moderate argillic alteration and incipient feldspar destruction (Fig. 5b), an intense argillic alteration with complete texture destruction (Fig. 5c), an advanced argillic alteration and incipient silicification, and a pronounced silicification or residual vuggy-quartz (Fig. 5d). Transit between lithologic types may be gradual or relatively abrupt in the field, defining a spatial zonation in the hydrothermal alteration.

The upper unaltered sequence of andesites and dacites are part of the Azufre Andesite and Cumbres Dacite, respectively. The Azufre Andesite is made up of subaerial lavas of andesite and minor dacite composition, porphyritic to aphanitic texture, little or no-vesicular, and with a massive to flow-banded internal structure. The Cumbres Dacite is composed of dacites and subordinately riodacites, in coherent facies of subaerial lavas, with a well-developed porphyritic texture and banded structure.

4.2. Macro and mesoscale structures

The spatial distribution of macrostructures deforming the Quevar Dacite, its volcanic basement, the lithocap and the hosting epithermal deposits is included in the structural map of Fig. 6. Structural analyses at all scales allow grouping structures into three main sets: (1) sub-vertical dykes and veins with epithermal mineralization; (2) strike-slip faults; and (3) normal faults. The appearance of these structures on the outcrop scale is shown in Fig. 7 and their stereographic projection in Fig. 8. Field examples of crosscutting relations between different mesostructures are displayed in Fig. 9.

4.2.1. Dykes and veins with epithermal Ag–Pb–Zn mineralization

Dykes and veins with epithermal Ag–Pb–Zn (Sb, As, Bi) mineralization occur along an ENE-trending band, which includes the Vince, Armonía and Quespejahuar deposits (Fig. 6). They present a dominant ENE-trend and a sub-vertical dip both towards the NW and SE (Fig. 8). However, the vein orientation can locally change to a NE/NNE and NW trend, as in the Vince deposit. At the outcrop scale, the individual veins have a millimeter to centimeter (<5 cm) thickness (Fig. 7a and b). Mineralized veins are grouped in swarms of subparallel structures whose thickness varies between 5 cm and 1 m, hosted in the Quevar Dacite with an argillic, advanced argillic and silicic hydrothermal alteration. In the Armonía deposit, mineralized vein swarms exhibit roughly subparallel silicification development.

4.2.2. Strike-slip faults

These brittle structures are organized into three sets of different orientation: (1) ENE to E-trending left-lateral strike-slip faults; (2) NW to NNW-trending left-lateral strike-slip faults; and (3) NNE to N-trending right-lateral strike-slip faults. All of them have a high-dip angle (>65°) and contain striations with a low-pitch angle (<25°; Fig. 8), Strike-slip faults have been observed at all scales affecting the Vince, Armonía and Quespejahuar mineral deposits (Figs. 6 and 9). The ENE to E-trending left-lateral strike-slip faults are cartographically dominant and are often disposed with an *en-échelon* map pattern, laterally connected by NW to NNW-trending left-lateral strike-slip faults. The NNE to N-trending right-lateral strike-slip faults are less developed at all scales. The local development of ENE to E-trending anticlinal and synclinal folds with large wavelength and sub-horizontal axes (Fig. 6) is spatially associated to this strike-slip deformation.

In the Quespejahuar and Armonía deposits, the strike-slip faults deform the dacites variably affected by the argillic and advanced argillic alterations, the subparallel silicified bands, and the mineralized veins (Fig. 7c, d, e). In some sectors of the advanced argillic alteration, the development of alunite aggregates elongated along the mesoscopic strike-slip faults is frequent, as well as filling subparallel tension gashes. Some fault planes exhibit fills and impregnations of oxides and oxy-

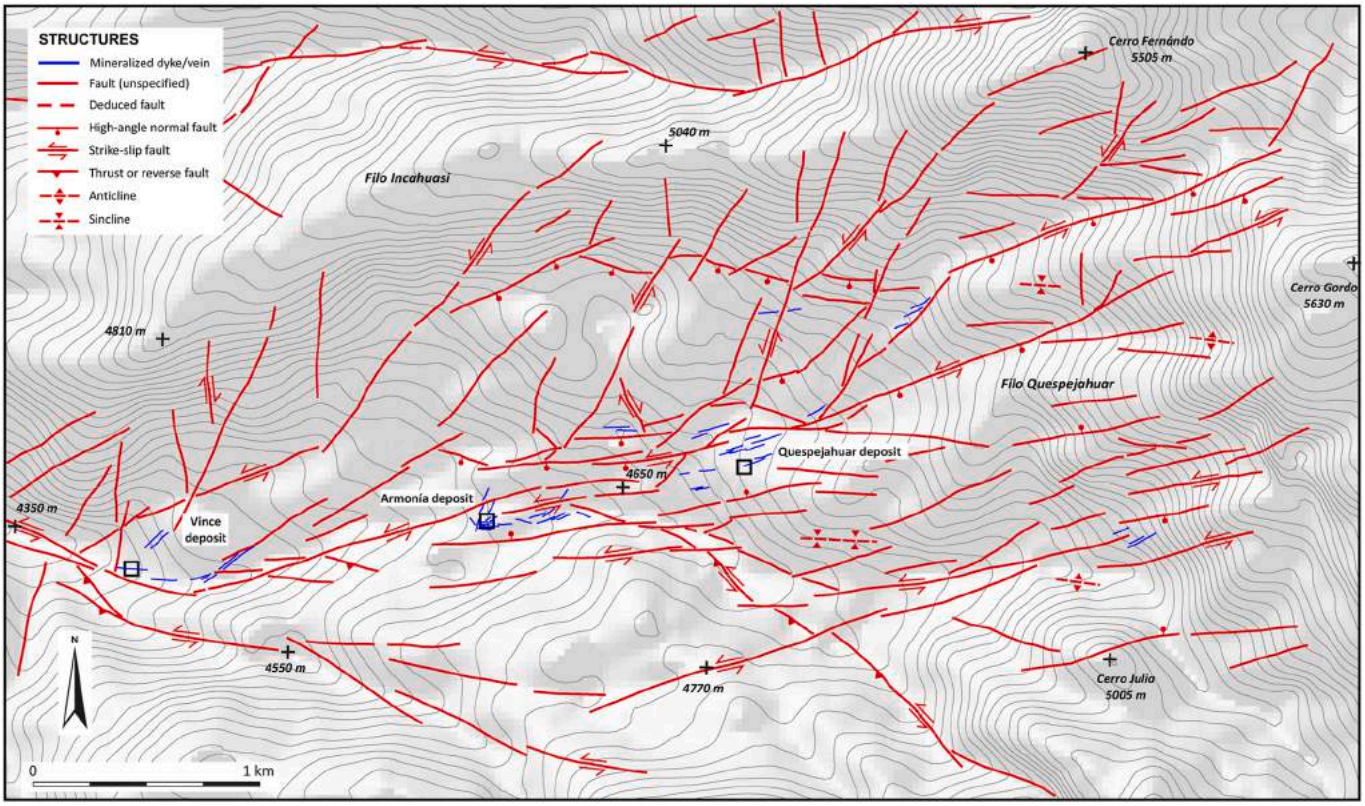

Fig. 6. Structural map of the Quebrada Incahuasi of the Quevar Volcanic Complex. Shaded relief in grayscale has been obtained made from the GMRT data-set with GeoMapApp (www.geomapapp.org).

hydroxides of Fe, which have resulted from the oxidation of the sulfide mineralization and the mobilization/precipitation of dissolved material within the fracture network (Escuder-Viruete et al., 2021).

4.2.3. Normal faults

The ENE to E and ESE-trending normal and oblique-normal faults exhibit high-dip angles towards the N and S (Fig. 8). These extensional structures have been observed at all scales, mainly on the southern slope of the Filo Incahuasi, along the Incahuasi valley, and in the sectors of the Armonía and Quespejahuar deposits. They produce important vertical block displacements and juxtapose rocks of different type and degree of hydrothermal alteration (Fig. 7h). On the southern slope of the Filo Incahuasi a normal fault system produced a vertical throw of about 75–100 m on the lava flows of the Azufre Andesite (Fig. 7f and g). In the Armonía and Quespejahuar deposits, the ENE to E-trending normal faults contain striations characterized by high-pitch angles (>60°), which indicate a direct normal movement or with a small strike-slip component (Fig. 8). In these sectors, normal faults deform argillic alteration, silicification and the hosted mineralized veins. These extensional structures coexist with the ENE to E-trending strike-slip faults at both map and outcrop scales, so that both types of structures can be kinematically related or result from successive deformation phases that occur over time. However, the reactivation of the strike-slip surfaces as normal faults, evidenced by high-pitch angle striations overprinting low-pitch angle striations on the same ENE to E-trending planes (Fig. 9), as well as the kinematical compatibility (see fault-slip data inversion section), imply the existence of two deformation events.

4.3. Stress field solutions obtained by inversion of mineralized veins and fault-slip data

Stress inversion of the mineralized vein sets and fault-slip data yield 11 stress tensors, whose geological characteristics and site locations in the Quebrada Incahuasi are reported in Appendix B, C and D. This compilation of stress tensors only includes data derived from veins and faults developed in volcanic rocks of late Miocene age. Appendix E includes the orientation of the maximum horizontal stress, stress regime, kinematic type of faults and the immersion method used in each site, which are generally consistent with each other.

4.3.1. Stress tensors obtained from the bingham distribution of mineralized dykes and veins

Fig. 8 shows the stereographic projection of the symmetry axes (ε_1, ε_2 and ε_3) of the Bingham distribution of mineralized dykes and veins in 6 locations of the Quebrada de Incahuasi, relative to the maximum, intermediate and minimum plane pole concentration. The characteristics of the corresponding stress tensors are summarized in Appendix C. Stress tensors present a dominant ENE to NE-trend for the maximum horizontal stress (σ_1) and a NNW to NW-trend for the minimum horizontal stress (σ_3), indicating that the Quebrada de Incahuasi was subjected to a strike-slip stress regime during the formation of the mineralized dykes and veins. The obtained sub-vertical orientation of the σ_2 stress axis is consistent with the frequent arrangement of mineralized veins in conjugate *en-échelon* systems in plan view, where the sub-horizontal σ_1 bisects the acute angle formed by the intersection of conjugate vein systems (Fig. 9). Sub-vertical mineralized structures were initially opened normal to the orientation of the sub-horizontal σ_3 stress axis, which presents a relatively homogeneous NNW to NW-trend in all studied sites.

4.3.2. Stress tensors obtained by inversion of fault-slip data

In the Quebrada Incahuasi, reduced stress tensors were calculated from fault-slip data measured in 5 sites located near the main strike-slip fault zones and around the mineral deposits. The stereographic projections of the obtained principal stress axes from several inversion methods at each geographic site are shown in Fig. 8. Paleostress analysis

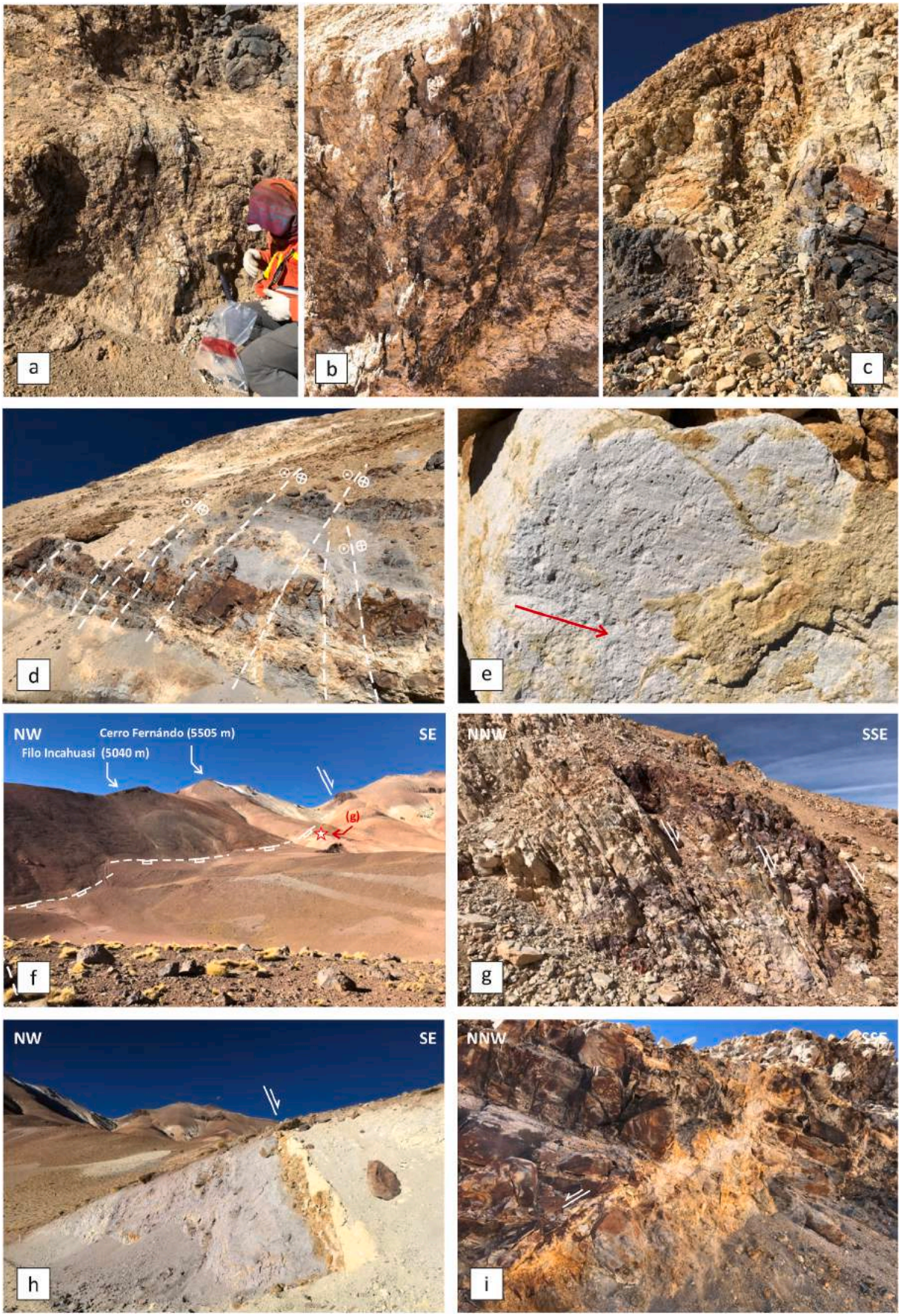

(caption on next page)

Fig. 7. Field photographs of tectonic structures developed in the volcanic rocks of the Quevar Dacite and hydrothermally altered equivalents. (a) Sub-vertical dykes and veins with high-sulfidation Ag–Pb–Zn mineralization at Armonía deposit. (b) Sub-vertical veins and pockets with mineralization hosted in a rockmass with advanced argillic alteration and limonitic impregnation. (c) Sub-vertical ENE-directed strike-slip fault that deforms and displace the epithermal mineralization in the Quespejahuar deposit. (d) System of subparallel left-laterall ENE to E-directed strike-slip faults that deform the argillic alteration and mineralized masses in the Armonía deposit. (e) Low pitch angle grooves lining a strike-slip fault plane developed in advanced argillic alteration. (f) Panoramic view showing the system of ENE-trending normal faults that runs along the southern slope of the Filo Incahuasi to the Abra del Viento pass. (g) Detail of normal faults and associated fractures developed in volcanic rocks with argillic alteration. See location in f. (h) Normal fault juxtaposing volcanic rocks with argillic alteration and alunite under rocks completely replaced by advanced argillic alteration. (i) Normal fault with subparallel development of atgillic alteration deforming moderately altered dacites.

was limited to the availability of rock outcrops with a sufficient number of fault-slip data, but the obtained results have allowed us to reconstruct the evolution of the stress regime in the late Miocene.

In the 18JE02 site of the Quespejahuar deposit, the stereographic projection of the fault planes and the low-pitch angle (<25°) of associated striae establishes that these are strike-slip faults (Appendix B). Aplication of the right-dihedra method to these strike-slip faults set gives a stress tensor whose principal stress axes σ_1, σ_2 and σ_3 have an orientation (and relative value) of N232°E/07 (0.49), N101°E/79 (0.32) and N323°E/08 (0.20), respectively. These results establish a NE-directed sub-horizontal shortening in a strike-slip regime (σ_2 is sub-vertical, R = 0.09), which is reflected in a sub-vertical intersection in the compression and extension dihedral diagram. Inversion of the fault-slip data using the direct inversion method yields a similar stress tensor. The trend of the principal strain axes obtained by numeric dynamic analysis is also compatible, with λ_1, λ_2 and λ_3 oriented N233°E/08, N066°E/82 and N323°E/02 (E = 0.5), respectively.

Fig. 8 shows the results of the inversion method in the 18JE05 site located in the Armonia deposit. Stereographic projection of fault-slip data establishes the existence of sub-vertical faults characterized by striations with low and high-pitch angles, which indicate strike-slip and normal movement, respectively. Stereographic projection of P and T kinematic axes of all fault-slip data shows a great dispersion (Appendix B). However, the distribution of these axes allows separating two fault subsets compatible with strike-slip (sub-horizontal P axes) and extensional (sub-vertical P axes) stress regimes. Application of the right-dihedra method to the strike-slip fault set gives a stress tensor whose main stress axes σ_1, σ_2 and σ_3 are N053°E/00 (0.48), N144°E/66 (0.31) and N322°E/24 (0.24), respectively. Similarly, the values for principal stress axes obtained for the normal fault subset are N066°E/88 (0.46), N261°E/02 (0.33) and N171°E/01 (0.21), respectively. Dihedral diagrams for each calculated stress tensor are characteristics of strike-slip and extensional faults. The application of the direct inversion method to the same fault sets gave rise to strike-slip and extensional tensors of very similar orientation. (Fig. 8). Using the numeric dynamic analysis for the strike-slip faults subpopulation, yields a compatible strain tensor of axes (λ_1, λ_2 and λ_3) trending N060°E/10, N194°E/75 and N328°E/10 (E = 0.55), respectively. Analogously, the principal strain axes obtained for the normal faults subpopulation are N045°E/88, N262°E/01 and N172°E/01 (E = 0.47). In summary, inversion of the fault-slip data establishes the existence of two different stress tensors in the 18JE05 site of late Miocene age. As field data indicate that high-pitch angle striations indicative of an extensional movement are superimposed to low-pitch angle striations formed during a strike-slip movement (Fig. 9), the extensional stress tensor is more recent in time.

The result of the inversion of fault-slip data in site 18JE13 located near the power keg of the Quespejahuar deposit is included in Fig. 8. The stereographic projection of the measured sub-vertical faults characterized by striations with high-pitch angle establishes that these are normal faults. Their kinematic axes indicates that they were formed during a single deformation phase (Appendix B). Application of the right-dihedra method establishes an orientation for σ_1, σ_2 and σ_3 of N069°E/59 (0.46), N273°E/29 (0.30) and N177°E/11 (0.24), respectively. These results define a sub-vertical compression under an extensional regime in the NNW trend (σ_1 is sub-vertical, R = 0.08), which is reflected in a sub-horizontal intersection in the compression and extension dihedral diagram (Fig. 8). Although independent of each other, the results obtained with the direct inversion and numeric dynamic analysis methods are compatible with right-dihedra method. For example, the trend of the main strain axes obtained by numeric dynamic analysis is N075°E/75, N267°E/15 and N177°E/03 (E = 0.32).

Fig. 8 shows how the inversion of fault-slip data in site 18JE16 located in the Arena sector of the Incahuasi river upper valley also yielded two stress tensors: a strike-slip regime under ENE-directed shortening and an extensional regime of NNW trend. Stereographic projection of fault-slip data establishes the existence of sub-vertical faults characterized by striations with low and high-pitch angles, which indicate strike-slip and normal displacements. Their kinematic axes shows a large dispersion without a single well-defined maximum (Appendix B). Application of the right-dihedra method to the strike-slip fault set gives a tensor of axes σ_1, σ_2 and σ_3 with trends N059°E/08 (0.48), N308°E/67 (0.31) and N152°E/21 (0.24), respectively. Similarly, the set of normal faults is compatible with a tensor of axes N091°E/71 (0.41), N241°E/16 (0.33) and N334°E/09 (0.26). The right dihedral diagrams for each fault set are characteristics of strike-slip and extensional faults (Fig. 8). Application of the direct inversion method leads to similar results, which establishes strike-slip and extensional deformation regimes for each fault set. The principal strain axes (λ_1, λ_2 and λ_3) obtained from numeric dynamic analysis for the strike-slip faults are N068°E/20, N278°E/67 and N162°E/11 (E = 0.59). Analogously, the strain tensor obtained from the normal faults is N087°E/80, N256°E/09 and N346°E/02 (E = 0.47). Therefore, the tensors obtained from the different inversion methods are compatible with each other.

5. ^{40}Ar–^{39}Ar geochronology

The main objective of geochronology was to obtain the ages of the Quevar Dacite, the hydrothermal alteration and the Ag–Pb–Zn epithermal mineralization, as well as indirectly the age of coeval tectonic deformation. To fulfill this objective, dacites affected by a different degree of hydrothermal alteration were sampled and separated volcanic and hydrothermal mineral fractions with different closure temperatures (in the sense of Hodges, 2003) were analyzed. A summary of sample location, ^{40}Ar-^{39}Ar incremental heating experiments and the ^{40}Ar-^{39}Ar spectrum and isochron diagrams of mineral separates are reported in Appendix F of the electronic supplementary material.

QV04 sample is a dacite collected in the lower stratigraphic levels of the Quevar Dacite at the Armonía deposit. It corresponds to pyroclastic facies, with ash to block-size clasts, affected by a moderate argillic alteration and incipient destruction of the feldspar. In the vicinity, there are hot springs with a clear structural control in relation to ENE-trending faults. The obtained biotite plateau age is 4.29 ± 0.29 Ma (MSWD = 0.33, probability = 0.81, 2σ, including a J-error of 0.4%) for four steps (6–9) of the incremental heating and 84.0% of the ^{39}Ar released (Fig. 10). The inverse isochron age on six points is 4.2 ± 1.2 Ma (MSWD = 0.25), with an initial ^{40}Ar-^{36}Ar intercept at 241 ± 25 Ma (Appendix F). The individual ages for the plateau have been calculated with the initial Ar ratio obtained from the isochron intersection. Although the collective interpretation of the geochronological results is addressed in a later section, given the late Miocene age of the Quevar Dacite (Robl et al., 2009), these results suggest the existence of a Zanclean age (early Pliocene) isotopic resetting thermal event, which reached temperatures above the biotite closure temperature (T ~ 400 °C) or, alternatively, the opening of the system during the hydrothermal alteration process.

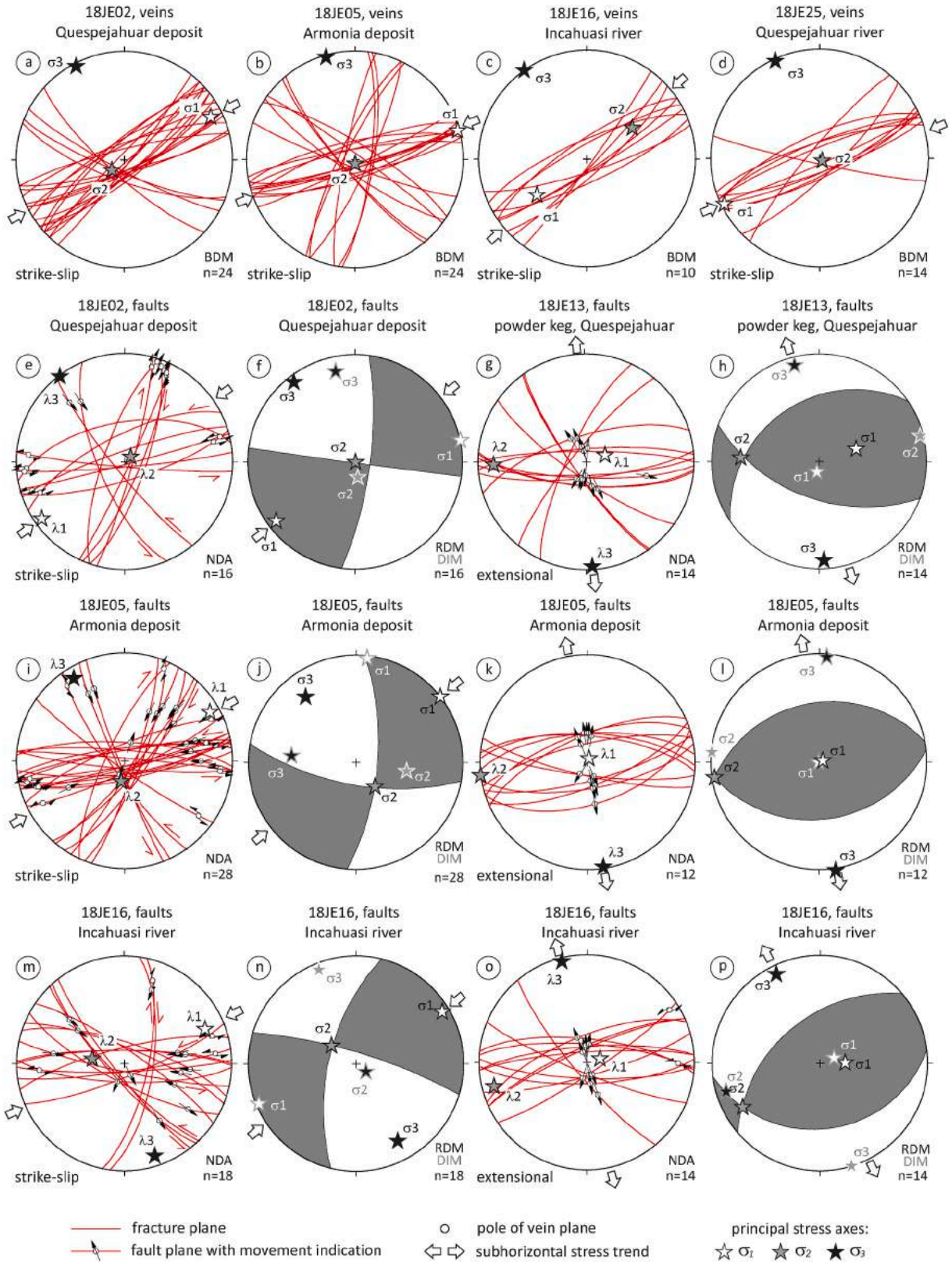

Fig. 8. Reduced stress tensors obtained by mineralized veins and fault-slip data inversion in the Quebrada Incahuasi (equal angle, lower hemisphere stereonets). (a to d) Stereoplots of the principal stress axis obtained from the Bingham distribution method (BDM) of mineralized dykes and veins. (e to p) Stereoplots of the principal stress axis, projection of striations in fault planes, compression (dark gray) and extension (white) dihedrals, and kinematic axes obtained from the right dihedral method (RDM), numerical dynamic analysis method (NDA) and direct inversion method (DIM). Inversion of fault-slip data was performed with the *TectonicsFP* software of Reiter and Acs (2000) and allows the identification of reduced stress tensors compatible con two tectonic regimes: an older strike-slip and a younger extensional.

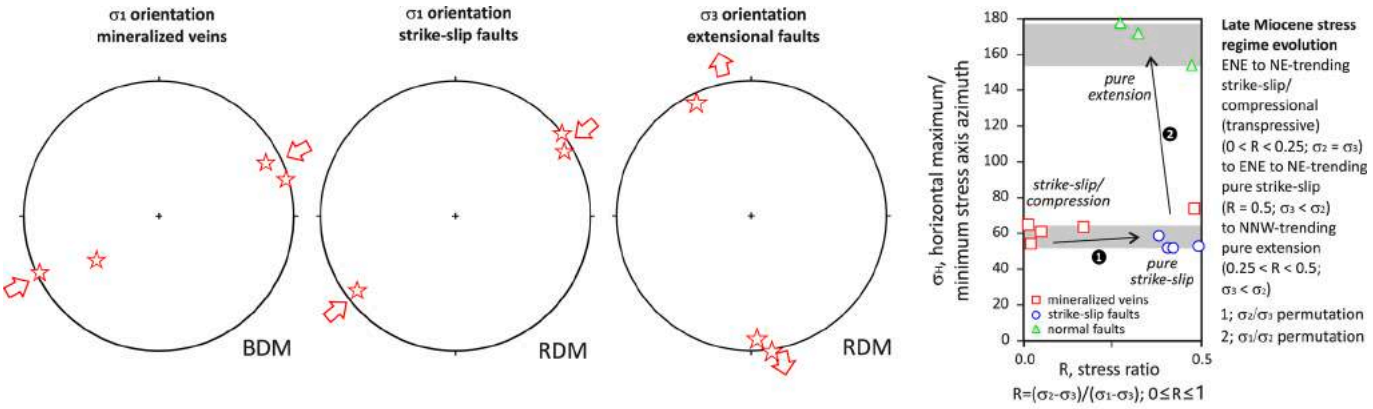

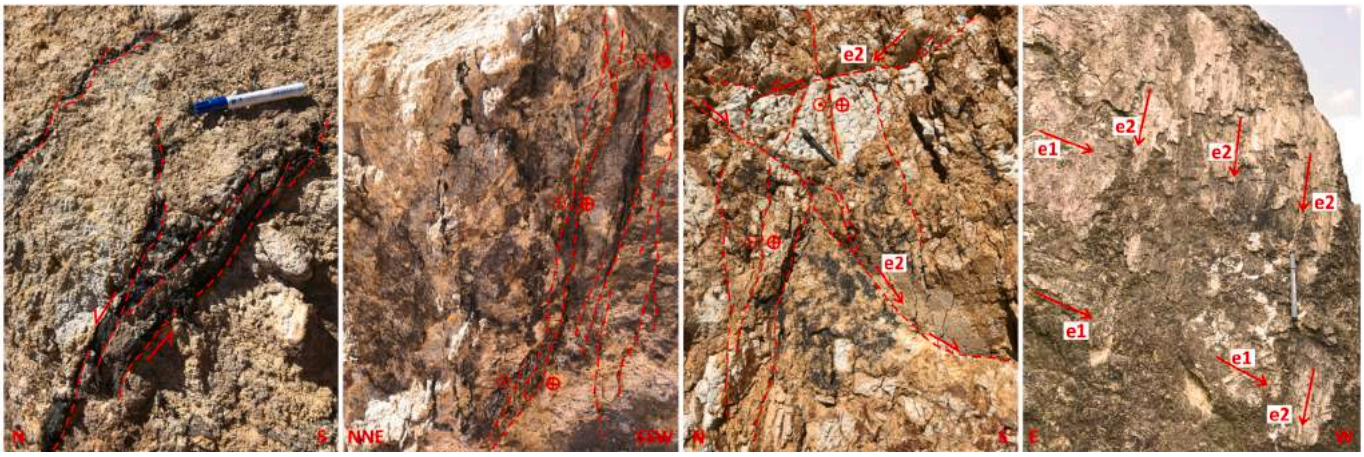

Fig. 9. (a) Stereoplots of principal stress-axes obtained from mineralized vein planes and fault-slip data inversion and (b) their classification according to its kinematic regime. Field examples of crosscutting relations between different mesostructures developed in the hydrothermally altered Quevar Dacite: (c) *en-échelon* mineralized vein system in plan view indicating a left-lateral strike-slip displacement; (d) system of sub-vertical mineralized veins reactivated as left-lateral strike-slip faults; (e) Sub-vertical left-lateral strike-slip faults cut by mid-to high-angle normal faults, which contain striations characterized by high-pitch angles (e2); and (f) reactivation of a strike-slip surface as a normal fault, evidenced by high-pitch angle striations (e2) overprinting low-pitch angle striations (e1) on the same ENE to E-trending plane.

A separate of the volcanic groundmass from QV04 sample has provided a plateau age of 9.63 ± 0.18 Ma (MSWD = 0.85, probability = 0.55) for eight steps and 77.4% of the ^{39}Ar released (Fig. 10). The inverse isochron age on eight points is 9.58 ± 0.34 Ma (MSWD = 0.92), with an initial ^{40}Ar-^{36}Ar intercept at 293 ± 18 Ma close to the atmospheric value (295.5). Given the quick cooling of the groundmass in volcanic conditions, the plateau age is an estimate of the extrusion age of the QV04 dacite in the Tortonian (late Miocene). A separate of plagioclase from sample QV04 has also provided a plateau age of 8.71 ± 0.53 Ma (MSWD = 0.65, probability = 0.74) for nine steps and 90.8% of the ^{39}Ar released (Fig. 10). The inverse isochron age on nine points is 9.4 ± 1.1 Ma (MSWD = 0.94), with an initial ^{40}Ar-^{36}Ar intercept at 284 ± 18 Ma. The rapid cooling of the felsic magma and the closing temperature of the plagioclase (T ~ 225 °C) suggest that this plateau age corresponds to the dacite extrusion in the Tortonian, which is similar, within the error, to those obtained for the groundmass.

QV10 sample is a porphyritic dacite lava, slightly affected by hydrothermal argillic alteration and devoid of mineralization. The sample was collected about 400 m SE of Quespejahuar deposit and represents the lower stratigraphic levels of the Quevar Dacite. The obtained biotite plateau age is 7.68 ± 0.37 Ma (MSWD = 0.32, probability = 0.90) for six steps and 85.4% of the ^{39}Ar released (Fig. 10). The inverse isochron age obtained for the four points with the lowest temperature is 11.4 ± 6.6 Ma, for an ^{40}Ar/^{36}Ar initial ratio of 78 ± 33 (MSWD = 18), which has a large error and is far from the atmospheric value. The inverse isochron age obtained for the six points of the highest temperature is 8.0 ± 1.7 Ma, for an initial ratio ^{40}Ar/^{36}Ar = 281 ± 70 (MSWD = 0.35), which is close to the atmospheric. Therefore, this age calculated from the high-T steps of the plateau is the best age estimation for biotite crystallization in the Tortonian. The inverse isochron on five first steps suggests Ar mobility through the mineral lattice causing a loss of ^{40}Ar at low temperatures.

A separate of the volcanic groundmass from QV10 sample has provided a plateau age of 9.91 ± 0.22 Ma (MSWD = 0.88, probability = 0.52) for eight steps and 81.8% of the ^{39}Ar released (Fig. 10). The older ages obtained in the higher temperature increments suggest incorporation of older material in the groundmass or an Ar excess. The inverse isochron age obtained for eight points is 9.87 ± 0.27 Ma, for an initial ratio ^{40}Ar/^{36}Ar = 309.8 ± 5.5 (MSWD = 0.8). Given the quick cooling of the groundmass under volcanic conditions, the plateau age probably corresponds to the extrusion age of the dacite in the Tortonian.

QV16B sample consists of a dacitic lava with small sulphide-mineralized veins and argillic alteration, collected at high stratigraphically levels of the Quevar Dacite. However, feldspar and biotite phenocrysts are apparently fresh. The obtained biotite plateau age is 6.44 ± 0.19 Ma (MSWD = 0.22, probability = 0.99) for eleven steps and 91.9% of the ^{39}Ar released (Fig. 10). The inverse isochron age obtained for ten points is 6.28 ± 0.49 Ma, for a ^{40}Ar/^{36}Ar initial ratio of 301 ± 17 (MSWD = 0.23), which is close to the atmospheric value. Therefore, the plateau and inverse isochron ages are similar. These results suggest the existence of a Messinian age (highest Miocene) thermal event with isotopic resetting, which reached temperatures higher than ~400 °C or, more likely, the opening of the system during the hydrothermal alteration process.

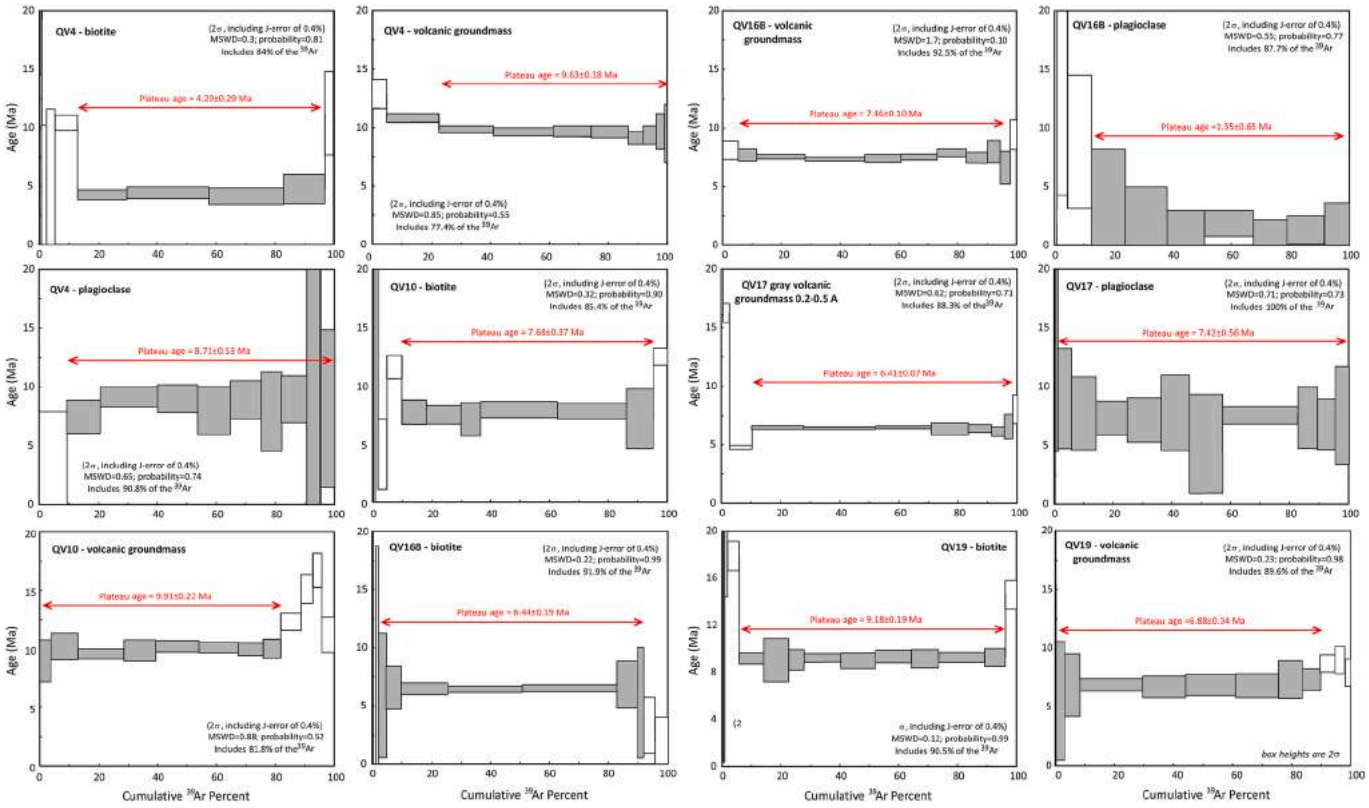

Fig. 10. $^{40}Ar/^{39}Ar$ spectrum of mineral separates from samples of unaltered and hydrothermally altered Quevar Dacite (isochron diagrams are included in Appendix F). All ages were obtained at the Pacific Centre Isotopic and Geochemical Research, Vancouver. Age uncertainties are 2σ and include uncertainty in monitor age and decay constant. See text for discussion.

A separate of the groundmass with hydrothermal minerals from sample QV16B has provided a plateau age of 7.46 ± 0.09 Ma (MSWD = 1.70, probability = 0.10) for nine steps and 92.5% of the ^{39}Ar released (Fig. 10). The inverse isochron age on ten points is 7.28 ± 0.18 Ma (MSWD = 1.5) for an initial ^{40}Ar-^{36}Ar intercept of 303.6 ± 7.8 Ma. Therefore, both ages coincide within the error. This sample has also provided a younger plagioclase plateau age of 1.35 ± 0.65 Ma (MSWD = 0.55, probability = 0.77), for seven steps and 87.7% of the ^{39}Ar released. Due to the probable opening of the isotopic system during the alteration processes of the dacite, the plateau age obtained for the volcanic groundmass of 7.46 ± 0.09 (Tortonian-Messinian boundary) can be an estimate for the age of the hydrothermal alteration.

QV17 sample is a dacitic lava related to autoclastic facies of monomictic breccia, affected by a minor argillic alteration. It is located in the upper stratigraphic levels of the Quevar Dacite, under the Azufre Andesite. A separate of the gray groundmass with hydrothermal minerals in the magnetic range of 0.2–0.5 A has provided a plateau age of 6.41 ± 0.07 Ma (MSWD = 0.62, probability = 0.71) for seven steps and 88.3% of the ^{39}Ar released (Fig. 10). The inverse isochron age for these seven points is 6.32 ± 0.33 Ma (MSWD = 0.74), for a low initial ^{40}Ar-^{36}Ar intercept at 226 ± 34. Although both ages coincide within the error, the best estimate of age is 6.32 ± 0.33 Ma, since the individual ages in the plateau were calculated with the initial Ar ratio obtained from the intersection of the inverse isochron.

In the same sample, a separate of the pink groundmass with hydrothermal phases in the magnetic range 0.5–1.0 A yielded a plateau age of 6.69 ± 0.10 Ma (MSWD = 1.09, probability = 0.36) for five steps and 72.8% of the ^{39}Ar released (Fig. 10). The corresponding age obtained by the inverse isochron method for eight points and a low initial ^{40}Ar-^{36}Ar intercept at 247 ± 25 (MSWD = 1.9) is 6.55 ± 0.33 Ma. This age is the best estimation for the sample, since the ages obtained in the plateau increments were calculated with the initial Ar relation obtained from the intersection of the inverse isochron. The four highest temperature increments provide an age by the inverse isochron method of 8.95 ± 0.48 (MSWD = 1.4), which suggests the existence of an older component in the volcanic groundmass and/or mobility of Ar through the rock.

Additionally, the QV17 sample yielded a plateau age for plagioclase of 7.42 ± 0.56 Ma (MSWD = 0.71, probability = 0.73), for 100% of the ^{39}Ar released in twelve steps of the incremental heating (Fig. 10). The similar age obtained by the inverse isochron method in the five high-T increments is 7.4 ± 1.2 Ma, for an initial ratio $^{40}Ar/^{36}Ar$ = 296 ± 62 (MSWD = 0.23) close to the atmospheric value. Taken together, the Messinian ages obtained in the QV17 sample suggest a thermal resetting event, which reached temperatures higher than 150 °C and/or an opening of the system during the hydrothermal alteration. Note that there are components in the groundmass of Tortonian age, similar to the extrusion ages obtained in other samples of the Quevar Dacite.

QV19 sample consist of a dacitic lava, moderately replaced by silicic and advanced argillic alteration. It contains mineralization dispersed in the rocks and filling fracture planes. The sample was collected at the highest stratigraphic levels of the Quevar Dacite. Biotite phenocrysts have provided a plateau age of 9.18 ± 0.19 Ma (MSWD = 0.12, probability = 0.99) for nine steps and 90.5% of the ^{39}Ar released (Fig. 10). The inverse isochron age obtained for nine points is 9.13 ± 0.40 Ma, for a $^{40}Ar/^{36}Ar$ initial ratio of 294 ± 20 (MSWD = 0.12), which is close to the atmospheric value. Therefore, both ages coincide within the error and account for the time of biotite crystallization by cooling during the magma extrusion in the Tortonian (late Miocene).

A separate of the groundmass with hydrothermal minerals in the magnetic range of 0.5–1.0 A yielded a plateau age of 6.88 ± 0.34 Ma (MSWD = 0.23, probability = 0.98) for eight steps and 89.6% of the ^{39}Ar released (Fig. 10). The age in the same groundmass separate obtained by the inverse isochron method for 7 points and an $^{40}Ar/^{36}Ar$ initial ratio of 293 ± 21 (MSWD = 0.10) is 6.78 ± 0.39 Ma. This age is similar to those

obtained in the pink groundmass of the QV17 sample. Analogously to this sample, the four highest temperature increments of the plateau provide an older age by the inverse isochron method of 8.2 ± 2.7 Ma, which also suggests the existence of an older component in the groundmass or the Ar mobility through the rock.

6. Discussion

6.1. Relationships between volcanic stratigraphy, hydrothermal alteration and epithermal mineralization

The field data in the Quebrada Incahuasi indicate that, after the rhyolitic dome emplacement of the Rhyolites and Perlites unit, the dacites and andesites of the Quevar Dacite were erupted. The accumulation of lava flows and pyroclastic deposits gave rise to the building of a large strato-volcano, during the late Miocene evolutionary stage of the QVC in the Central Andean Volcanic Zone. The volcanic mineralogy, textures and structures of the Quevar Dacite were later modified by the superposition of an hydrothermal alteration. In the Quebrada Incahuasi, the map distribution of this hydrothermal alteration defines the steeply-dipping structural root of the lithocap, which follows an ENE-trending band that includes the Vince, Armonía and Quespejahuar mineral deposits (Fig. 3). Therefore, the upflow of the magmatic-hydrothermal fluid from the deeper-seated source to the lithocap environment was structurally controlled by the ENE-trending fault zones. However, the lithocap is composed of a large sub-horizontal lenticular domain in excess of 1 km-thick, between the topographic heights of 4550 m (Vince deposit) and 5700 m (Cerro Azufre), extending laterally up to 10 km in the N and NE trends, along the Quebrada Toro Grande and Mamaturi (Marquetti et al., 2017). Therefore, the lateral outflow of the magmatic-hydrothermal fluid occurred when the ascending fluid reached its neutral buoyancy level and encountered a permeable stratigraphic aquifer, as the poorly consolidated volcaniclastic breccias and tuffs of the Quevar Dacite.

The lithocap hosts the high-sulfidation epithermal mineralization (Robl et al., 2009), which appears forming (1) dykes, veins and/or breccia cement and (2) more disseminated stratabound replacements. Mineralization in veins and breccia cements is mainly related to ENE-trending fault planes and sub-vertical fracture systems, located in the structural roots of the lithocap, as in the Vince, Armonía and Quespejahuar deposits. Therefore, this style of mineralization had a clear structural control. Reactivation of veins as faults during episodic deformation can result in several stages of tectonic brecciation, mineralization disruption and new infill of the created open spaces. Mineralization by replacement is generally located at a higher topographic elevation in the QVC. It is volumetrically much more extensive and typically hosted as replacements in the residual quartz domains. The extent of this type of mineralization was probably controlled by the lateral flow of mineralizing fluids (Escuder-Viruete et al., 2021).

The coherent facies of the Azufre Andesite and Cumbres Dacite unconformably overlap the Quevar Dacite, or hydrothermally altered rock equivalents. The field data imply: (a) an interruption of felsic volcanism; (b) the cessation of the hydrothermal alteration system and the high sulfidation mineralization; (c) the beginning of a stage of erosion of the volcanic edifice with the formation of a paleorelief; (d) the exposure of deep levels of the volcanic stratigraphy and lithocap that are brought close to the surface; and (e) a new reactivation of silicic magmatism in the QVC with the eruption of subaerial lavas. The erosion and formation of an erosive surface controlled the late gossan-type alteration, which has been preserved in the topographically higher sectors of the Quevar Dacite.

6.2. Late miocene structures in the Quebrada Incahuasi of the QVC

In the study area, the most prominent structure is the Calama-Olacapato-El Toro lineament, which both includes NW-trending segmented left-lateral strike-slip faults and broad bands of distributed shear deformation (Fig. 1). The lateral limits of the COT lineament are constituted by the Quevar and Chorrillos left-lateral strike-slip fault zones (Fig. 2; Acocella et al., 2011; Lanza et al., 2013). Both large-scale fault zones, together with other related lower-order structures, define a tectonic left-lateral strike-slip stepover at regional-scale (Seggiaro et al., 2016), which controlled the evolution of the Aguas Calientes caldera and the Quevar Volcanic Complex in the late Miocene, as well as the location of the mineralized veins in the Quevar and La Poma districts (Seggiaro et al., 2021). Thus, the main WNW-trending Quevar fault zone defines the southwestern boundary of the stepover. Internally, the stepover is divided by related subsidiary faults into smaller tectonic blocks.

In the Quebrada de Incahuasi, the geometric and kinematic analysis of faults carried out in this work indicates that the E to ENE-directed regional sub-horizontal shortening could have (re)activated the Quevar fault zone as a left-lateral strike-slip fault (Fig. 6). Angular relations between the main Quevar fault zone and ENE to E-trending left-lateral strike-slip faults, suggest that these subsidiary faults correspond to synthetic R-type structures (*sensu* Schreurs, 2003) laterally connected to the Quevar master structure. Therefore, the Quevar fault zone accommodated only a portion of the far stress field, whereas the remained was transferred as a near-field stress to ENE to E-trending R-type faults and left-lateral strike-slip duplexes (*sensu* Woodcock and Fisher, 1986) at several scales. These R-type faults juxtapose zones with different degrees of alteration in the lithocap, as well as control the tectonic landscape of elongate valleys in the Quebrada Incahuasi. Although development of NNW to N-trending, right-lateral strike-slip faults is rather limited in the Quebrada Incahuasi, the general trend of these structures with respect to the orientation of the external stress field suggests that these correspond to antithetical R′-type structures. Therefore, R and R′-type structures were able to accommodate a part of the far stress field through the internal disruption of the stepover into small tectonic blocks and, probably, a minor contribution through rotation and/or translation of such blocks.

On the other hand, the dykes and veins with epithermal Ag–Pb–Zn mineralization have a sub-vertical dip and a dominant ENE to NE trend, although in the Vince and Armonia deposits vein plane orientation ranges to a NNE strike (Fig. 8). Comparison between the orientation of the far stress field and the general trend of the mineralized structures suggests that they are favorably oriented T-type structures. This is consistent with the existence of open space fill textures in mineralized veins and associated fracture systems, opened by a NNW-trending orthogonal extension. In turn, the contact between the mineralized veins and the hosting altered dacite frequently exhibits a reactivation as a brittle fault (Fig. 9), in which the kinematic indicators in these planes establish both strike-slip and normal movements.

In summary, the epithermal mineralization in sub-vertical veins had a clear structural control, resulting from a general left-lateral strike-slip regimen, which gave rise to the opening of the ENE to NE-trending dykes and veins that channeled the mineralizing fluids. Furthermore, the different strike-slip fault sets distinguished in the Quebrada Incahuasi were also formed by a similar WNW-trending left-lateral strike-slip regime. Therefore, epithermal mineralization, associated hydrothermal alteration and strike-slip faulting are part of a progressive deformation, consequence of the regional stress field imposed by the E to ENE-directed convergence. On a larger scale, this progressive deformation was related to the formation of a left-lateral strike-slip stepover, produced between the Quevar and Chorrillos fault zones of the COT lineament (Acocella et al., 2011; Lanza et al., 2013; Seggiaro et al., 2016). The fault zones developed in Quebrada Incahuasi are thus integrated into the rhomboidally shaped stepover, or zone of slip transfer, between these overstepping and subparallel strike-slip faults.

The Azufre Andesite and Cumbres Dacite are not hydrothermally altered and apparently only deformed by normal faults. Therefore, the eruption of these subaerial lavas marks cessation of hydrothermal

activity and strike-slip motion along the COT, as well as the transition to an extensional or transtensive regional stress regime. This transition is documented by analyzing fault-slip data in the next section.

6.3. Late miocene tectonic stress regimes obtained from fault-slip data

In the Quebrada de Incahuasi, stress field solutions calculated from inversion of measured fault-slip data establish late Miocene strike-slip and extensional stress regimes, which are summarized in Fig. 9. Strike-slip stress regimes (σ_2 disposed sub-vertical) obtained from strike-slip faults are characterized by ENE to NE-trending maximum horizontal stress ($\sigma_H = \sigma_1$) and stress ratio values of $0.37 < R < 0.48$ (Appendix C), that establish a pure strike-slip type of deformation. The ENE to NE-trending sub-horizontal shortening was oblique to the WNW-ESE trend of the Quevar and Chorrillos fault zones of the COT lineament (Acocella et al., 2011; Lanza et al., 2013; Seggiaro et al., 2016). This obliquity resulted in the partition of the deformation inside the rhomboidally shaped stepover located between them, producing a left-lateral slip in the WNW and ENE/E faults (P and R-types) and a right-lateral slip in the NNW/N faults (R′-type).

The stress tensors obtained from the Bingham distribution of mineralized dykes and veins are characterized by the ENE to NE-trending of the maximum horizontal stress (σ_1) and values of the stress ratio between $0.02 < R < 0.16$ (a value equal to 0.47; Fig. 9). Therefore, the prevailing stress regime during the formation of the epithermal Ag–Pb–Zn mineralizations was strike-slip/compressional ($R < 0.25$; $\sigma_2 = \sigma_3$). The σ1 trend is subparallel to that of the mineralized dykes and veins, so their opening as T-type structures could have taken place during this tectonic regime. The internal tectonic brecciation of the veins, with successive stages of cementation and mineralization of the resulting matrix, and the reactivation of the vein-wallrock contact as a strike-slip fault indicate that the strike-slip was coeval and subsequent to mineralization. Therefore, the obtained stress regimes support the interpretation that formation of mineralized veins, their subsequent reactivation as strike-slip faults and the formation of the different kinematic fault-sets are different stages of a progressive deformation under a similar strike-slip regime. The change from a strike-slip/compression to a pure strike-slip regime, recorded by the R-value increase, is interpreted as related to a permutation (*sensu* Peacock et al., 2017b) of σ_3 into σ_2 vertical stress (Fig. 9).

Extensional stress regimes (σ_1 disposed sub-vertical) obtained from normal and oblique-normal faults are characterized by NNW to N-trending minimum horizontal stress (σ_3) and stress ratio values of $0.27 < R < 0.47$ (Appendix C), that establish a pure extension type of deformation (Fig. 9). Field crosscutting relationship and timing of fault movement indicate in several locations (as Armonia and Quespejahuar deposits) an initial left-lateral strike-slip movement along ENE to E-trending faults caused by the strike-slip regime, followed by a normal movement in the same fault surfaces triggered by the extensional regime (Fig. 9). The strike-slip regime prevails until the eruption of the Azufre Andesite and Cumbres Dacite, which are only deformed by normal faults. Therefore, in Quebrada Incahuasi, the extensional regime replaces that of strike-slip, and it does so prior to the eruption of these units. The change from a pure strike-slip to a pure extensional was related to a permutation of the vertical stress from σ_2 to σ_1 (Fig. 9).

6.4. Age of the Quevar Dacite and hydrothermal alteration in the Quebrada Incauhasi

Fig. 11 summarizes the ^{40}Ar-^{39}Ar geochronological results obtained for Quevar Dacite samples in the Quebrada Incahuasi of the QVC. The oldest obtained ages were in the biotite phenocrysts of the QV19 sample, which belongs to the highest stratigraphical levels of the unit that were apparently not affected by the hydrothermal alteration. This age is interpreted as that of biotite crystallization by cooling during the magma eruption in the Tortonian (late Miocene). The plateau and inverse isochron ages obtained for the rest of the biotites in rocks affected by hydrothermal argillic alteration (QV4 and QV10) are younger, although they were collected at lower levels of the volcanic sequence. These results suggest the existence of a Messinian age (latest Miocene) thermal event with isotopic resetting, which reached temperatures above the biotite closure temperature (T ~ 400 °C) or, more likely, the opening of the system during hydrothermal alteration processes.

However, the plagioclase phenocrysts from the QV4 sample have provided relatively older ages, similar within error to those obtained in the biotite phenocrysts from the QV19 sample. Therefore, this age also records the plagioclase crystallization by cooling during the magma eruption in the Tortonian. The rest of the plagioclase have provided younger plateau and inverse isochron ages. These ages were obtained in samples collected at the highest stratigraphic levels of the Quevar Dacite, which contain sulphide-mineralized veins and are variably affected by hydrothermal argillic alteration (QV16B and QV17). Therefore, these Messinian ages are related to a thermal resetting event, which reached T > 150 °C (plagioclase closure temperature; Hodges, 2003) and/or to a system opening during the hydrothermal alteration.

Separates from the volcanic groundmass have also provided

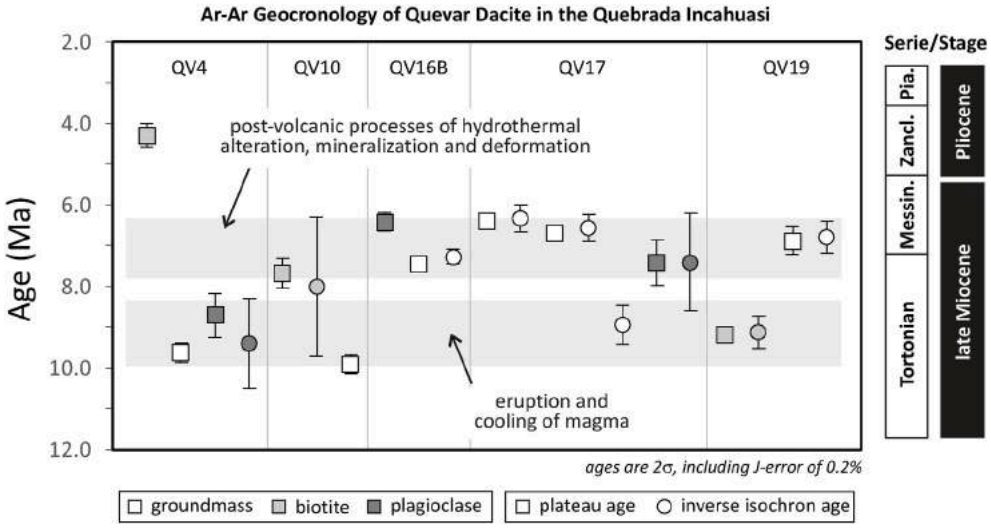

Fig. 11. Summary of the ^{40}Ar-^{39}Ar geochronological results obtained for mineral separates and volcanic groundmass in samples of the Quevar Dacite. See explanation in text.

relatively old plateau ages (QV4 and QV10), similar within error or slightly older than those obtained in part of the biotite and plagioclase phenocrysts. Although these samples are slightly affected by hydrothermal argillic alteration, they have preserved the primary isotopic values and the resulting age is interpreted as corresponding to the rapid cooling of the dacitic magma during the eruption. In favor of this interpretation is the inverse isochron age obtained in the four highest temperature increments for the pink groundmass in the QV17 sample, which suggests the existence of an older component in the volcanic groundmass. The rest of the plateau and inverse isochron ages obtained in the groundmass fall in the 7.46 to 6.32 Ma interval (latest Miocene). These relatively young ages were obtained in samples with veins and disseminated sulphide mineralization, as well as variably replaced by silicic and advanced argillic alteration (QV16B, QV17 and QV19). As in the case of the younger age group obtained in the biotite and plagioclase phenocrysts, these ages record the opening of the isotopic system during the hydrothermal alteration and epithermal mineralization processes in the Quevar Dacite.

6.5. Late miocene evolution of the QVC

In this section, a structural evolutive model is proposed that integrates all data obtained in the Quebrada de Incahuasi of the Quevar Volcanic Complex. This model allows establishing the relationships between dacitic volcanism, hydrothermal alteration, epithermal mineralizations and coeval deformation. The model comprises three main stages schematically shown in Fig. 12.

The first stage included the eruption of the Quevar Dacite in the Tortonian (9.9–8.7 Ma) over the Aguas Calientes caldera ignimbrites (10.3 ± 0.3 Ma), within the evolutionary context of the Quevar Volcanic Complex. The construction of the volcanic complex took place through the accumulation of lavas and pyroclastic deposits, together with the syn-volcanic intrusion of subaerial felsic domes and/or crypto domes (Fig. 12a). The coherent facies consisted of dacitic and subordinately andesitic and riodacitic lavas, as well as autoclastic rim facies, and the pyroclastic facies included proximal monomictic block and ash flows deposits, and distal scoria and ash flow deposits. The regional WNW to NW alignment of the contemporary Rincón, Tul-Tul, Del Medio, Quevar and Azufrero volcanoes indicates a control of the COT lineament in the volcanic activity during this stage.

The second stage included the implantation of an extensive hydrothermal alteration system in the Quevar Dacite and the related formation of the epithermal Ag–Pb–Zn mineralization in the Messinian (7.7–6.3 Ma). The geometric and kinematic characteristics of the mineralized dykes and veins, the mineralized breccia zones and the related hydrothermal alteration (silicic, advanced argillic, argillic), indicate that the alteration and mineralization processes took place during a regional strike-slip deformation. This deformation was related to ENE to E-directed sub-horizontal shortening induced by Cenozoic regional convergence and the (re)activation of the Quevar fault system of the COT, which formed a large-scale left-lateral strike-slip stepover between WNW-trending regional faults (Fig. 12b). In the Quebrada Incahuasi, the internal deformation in the stepover produced mainly synthetic ENE to E-trending left-lateral strike-slip faults (R) and NNW to N-trending right-lateral strike-slip faults (R′), as well as the opening of ENE-trending planes (T) that host most of the mineralized dykes and veins. The main mineral deposits are included in an ENE-directed band that probably channeled the ascent of the magmatic-hydrothermal fluids.

The third stage included the erosion of the volcanic edifice and the lithocap, as well as the mobilization of chemical elements in relation to a supergenic alteration (gossan). The hydrothermal system ceased its activity prior to the eruption of the unaltered Azufre Andesite and Cumbres Dacite. In Quebrada Incahuasi, the kinematics of the brittle reactivation of mineralized veins and ENE-trending strike-slip faults indicate the subsequent implantation of a NNW-directed extensional regime. In this sector, ENE to E and WNW-trending extensional faults control the morphology and the incision of the drainage network.

The tectonic stress evolution of the QVC included a first regime of strike-slip/compression to a pure strike-slip, which was followed by a regime of pure extension. The successive changes in the stress regime were related to a permutation of σ_3 into σ_2 and after σ_2 into σ_1 vertical stress. The timing for the orogen-normal strike-slip stress regime ranges between ~10 and 6.5 Ma and the orogen-parallel extensional stress regime started in the latest Miocene (<6.5 Ma). This evolution of the regional stress regime during the Cenozoic is similar to that previously described in various sectors of the Antiplano-Puna plateau, Western Cordillera and along the Andes of southern and central Peru (Sébrier et al., 1988; Marrett et al., 1994; Cladouhos et al., 1994; Marrett and Strecker, 2000; Elger et al., 2005; Lanza et al., 2013; Daxberger and Riller, 2015; Giambiagi et al., 2016).

7. Conclusions

In the Quebrada Incahuasi of the QVC, the epithermal Ag–Pb–Zn mineralization in sub-vertical dykes and veins of the Vince, Armonía and Quespejahuar deposits, associated hydrothermal alteration and strike-slip faulting are part of a progressive deformation, consequence of the regional stress field imposed by the E to ENE-directed convergence. This progressive deformation was related to the formation of a left-lateral strike-slip stepover between the Quevar and Chorrillos fault zones of the COT lineament.

There are two age groups in the Quevar Dacite: (1) ages between 9.9 and 8.7 Ma (Tortonian) for syn-volcanic processes such as crystallization of phenocrysts and rapid cooling of the groundmass; and (2) ages between 7.7 and 6.3 Ma (Messinian) for post-volcanic processes that imply mobility of Ar through the rock produced by the opening of the system and/or thermal events with isotopic resetting at temperatures higher than the closing of each mineral. Therefore, the first group dates the time interval of Quevar Dacite eruption and the second group the hydrothermal alteration and epithermal mineralization.

The evolution of the stress regime recorded in the QVC during the Cenozoic has been interpreted regionally in terms of two main geodynamic phases: (1) an orogenic constructional phase, older than late Miocene, and (2) a gravitational collapse phase, active from late Miocene to present. The discussion of possible causes for the stress regime change in the northern Puna plateau exceeds the objectives of this work, focused on a sector of the QVC. However, this work documents how the transition from a strike-slip to an extensional regime led to an important hydrothermal alteration and epithermal mineralization in Quebrada de Incahuasi, as well as other coeval mineralizations described in the northern Puna, which illustrate why structural geology is critical to finding, evaluating and mining ore deposits.

Credit author statement

Javier Escuder Viruete: Conceptualization, Methodology, Formal analysis, Investigation, Writing- Original draft preparation, Project administration, Funding acquisition, Eduardo A. Molina: Conceptualization, Methodology, Formal analysis, Investigation, Writing - Review & Editing, Darío Chinchilla: Conceptualization, Methodology, Formal analysis, Investigation, Writing - Review & Editing, Janet Gabites: Methodology, Investigation, Writing - Review & Editing, Raúl Seggiaro: Investigation, Writing - Review & Editing, Project administration, Funding acquisition, Cintia A. Marquetti: Nemesio Heredia: Investigation, Writing - Review & Editing, Project administration, Funding acquisition.

Declaration of competing interest

The authors declare that they have no known competing financial interests or personal relationships that could have appeared to influence

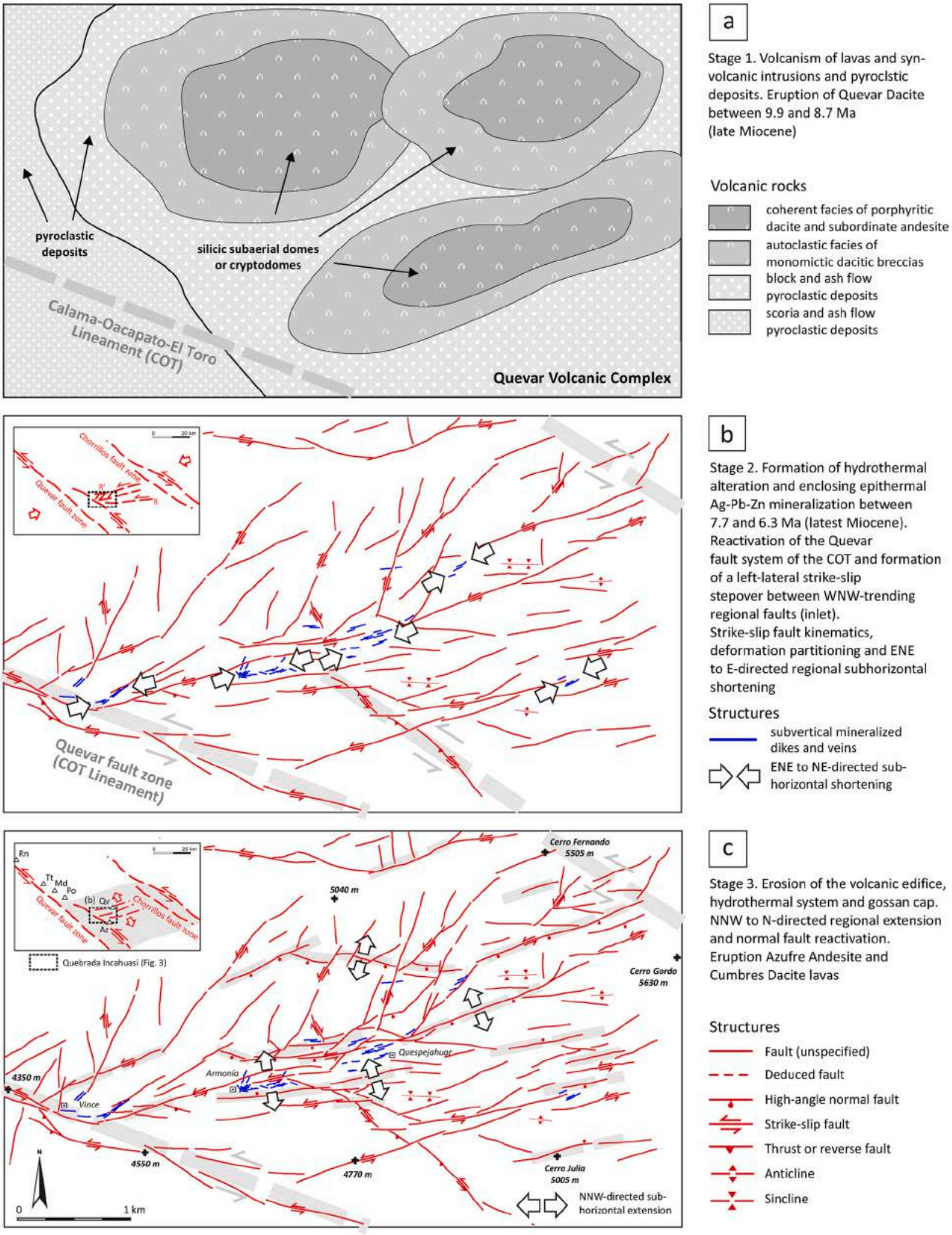

Fig. 12. Structural evolutive model of the Quevar Volcanic Complex in the Quebrada Incahuasi. In relation to eruption of Quevar Dacite, three stages are distinguished: (a) syn-volcanic in the Tortonian (late Miocene); (b) tardi-to post-volcanic with formation of epithermal mineralization and strike-slip faulting in the Messinian (latest Miocene); and (c) post-volcanic with extensional faulting and erosion. Inlet in (b) show the location of the Quebrada Incahuasi in the regional context of a tectonic left-lateral strike-slip stepover between WNW-trending regional faults of the COT. Volcanoes: Az; Azufrero, Rn; Rincón, TT; Tul-Tul, Md; Del Medio, Po; Pocitos, and Qv; Quevar.

the work reported in this paper.

Acknowledgments

We would like to thank the support and infrastructure provided by the *Servicio Geológico Argentino*, particularly to Raúl Seggiaro of the Provincial Delegation in Salta. We also greatly appreciate the facilities and logistical support during the field work to the Silex Argentina Company, concessionaire of the Quevar Mining Project. The involvement in X-ray diffraction analysis of Begoña del Moral (IGME-CSIC laboratories) is gratefully acknowledged. Careful and constructive reviews by Enrico Tavarnelli and Federico Rossetti, as well as the editorial work by Fabrizio Agosta, significantly improved the manuscript. The research was mainly funded by the MISAC project (32.0.00.66.00) under the Cooperation and Technical Assistance Agreement SEGEMAR-IGME. Some aspects of the research were funded through PID2019-105625RB-C22 project of the MCIN/AEI/10.13039/501100011033.

Appendix A. Supplementary data

Supplementary data to this article can be found online at https://doi.org/10.1016/j.jsg.2022.104582.

References

Acocella, V., Gioncada, A., Omarini, R., Riller, U., Mazzuoli, R., Vezzoli, L., 2011. Tectonomagmatic characteristics of the back-arc portion of the Calama-Olacapato-el Toro fault zone, central Andes. Tectonics 30, 3005. TC.

Allmendinger, R.W., Strecker, M., Eremchuk, J.M., Francis, P., 1989. Neotectonic deformation of the southern Puna Plateau, northwestern Argentina. J. S. Am. Earth Sci. 2, 111–130.

Allmendinger, R., Jordan, T., Kay, S., Isacks, B., 1997. The evolution of the Altiplano-Puna plateau of the central Andes. Annu. Rev. Earth Planet Sci. 25, 139–174.

Angelier, J., 1994. Fault slip analysis and paleostress reconstruction. In: Hancock, P. (Ed.), Continental Deformation. Pergamon Press, United Kingdom, pp. 53–100.

Bonnet, E., Bour, O., Odling, N.E., Davy, P., Main, I., Cowie, P., Berkowitz, B., 2001. Scaling of fracture systems in geological media. Rev. Geophys. 39, 347–383.

Célérier, B., Etchecopar, A., Bergerat, F., Vergely, P., Arthaud, F., Laurent, P., 2012. Inferring stress from faulting: from early concepts to inverse methods. Tectonophysics 581, 206–219.

Chernicoff, C.J., Richards, J.P., Zappettini, E.O., 2002. Crustal lineament control on magmatism and mineralization in northwestern Argentina: geological, geophysical, and remote sensing evidence. Ore Geol. Rev. 21, 127–155.

Cladouhos, T.T., Allmendinger, R.W., Coira, B., Farrar, E., 1994. Late Cenozoic deformation in the Central Andes: fault kinematic from the northern Puna, northwestern Argentina and southwestern Bolivia. J. S. Am. Earth Sci. 7, 209–228.

Cohen, K., Finney, S., Gibbard, P., Fan, J.X., 2013. The ICS international chronostratigraphic chart. Episodes 36, 199–204. https://doi.org/10.18814/epiiugs/2013/v36i3/002.

Cooke, D.R., Hollings, P., Wilkinson, J.J., Tosdal, R.M., 2014. Geochemistry of porphyry deposits. In: Heinrich, D., Holland, K., Turekian, K. (Eds.), Treatise on Geochemistry, second ed. Elsevier, pp. 357–381.

Cowie, P.A., Sornette, D., Vanneste, C., 1995. Multifractal scaling properties of a growing fault population. Geophys. J. Int. 122, 457–469.

Cox, S.F., 2005. Coupling between deformation, fluid pressures and fluid flow in ore producing hydrothermal systems at depth in the crust. Econ. Geol. ume, 1–35.

Davis, B., 2002. Microstructural analysis. In: Vearncombe, S. (Ed.), Applied Structural Geology for Exploration and Mining, vol. 36. Australian Institute of Geoscientists Bulletin, p. 242.

Daxberger, H., Riller, U., 2015. Kinematics of Neogene to Recent upper-crustal deformation in the southern central Andes (23°-28° S) inferred from fault-slip analysis: evidence for gravitational spreading of the Puna Plateau. Tectonophysics 642, 16–28.

de Silva, S.L., Kay, S.M., 2018. Turning up the heat: high-flux magmatism in the Central Andes. Elements 14, 245–250.

Elger, K., Oncken, O., Glodny, J., 2005. Plateau-style accumulation of deformation: Southern Altiplano. Tectonics 24 (TC4020). https://doi.org/10.1029/2004TC001675.

Escuder Viruete, J., Molina, E.A., Chinchilla Benavides, D., Gabites, J., Seggiaro, R., Heredia Carballo, N., Marquetti, C.A., 2021. Evaluación metalogenética y estudio geológico-estructural del distrito polimetálico de San Antonio de los Cobres, provincias de Salta y Jujuy, República Argentina. Parte II: características estructurales y edad de las mineralizaciones y alteraciones asociadas en la Quebrada de Incahuasi del Complejo Volcánico Quevar. Contrib. Técnica Recur. Miner. 46, 84. ISSN 2618-5032. https://repositorio.segemar.gov.ar/handle/308849217/4182.

Giambiagi, L., Alvarez, P., Spagnotto, S., 2016. Temporal variation of the stress field during the construction of the central Andes: constrains from the volcanic arc region (22–26° S), Western Cordillera, Chile, during the last 20 Ma. Tectonics 35, 2014–2033.

Grosse, P., Guzmán, S., Petrinovic, I.A., 2017. Volcanes compuestos cenozoicos del noroeste argentino. In: Muruaga, C.M., Grosse, P. (Eds.), Ciencias de la Tierra y Recursos Naturales del NOA. Relatorio del XX Congreso Geológico Argentino. San Miguel de Tucumán, pp. 484–517.

Guzmán, S., Grosse, P., Montero-López, C., Hongn, F., Pilger, R., Petrinovic, I., Seggiaro, R., Aramayo, A., 2014. Spatial-temporal distribution of explosive volcanism in the 25-28° S segment of the andean central volcanic zone. Tectonophysics 636, 170–189.

Guzmán, S., Grosse, P., Martí, J., Petrinovic, I., Seggiaro, R., 2017. Calderas cenozoicas argentinas de la zona volcánica central de los Andes - procesos eruptivos y dinámica: una revisión. In: Muruaga, C.M., Grosse, P. (Eds.), Ciencias de la Tierra y Recursos Naturales del NOA. Relatorio del XX Congreso Geológico Argentino. San Miguel de Tucumán, pp. 518–547.

Hedenquist, J., Arribas, A., 2017. Epithermal ore deposits: first-order features relevant to exploration and assessment. In: Proc. Of the 14th SGA Biennial Meeting 2017 Mineral Resources to Discover, vol. 1, pp. 47–50. Quebec City, Canada.

Hedenquist, J.W., Taran, Y.A., 2013. Modeling the formation of advanced argillic lithocaps: volcanic vapor condensation above porphyry intrusions. Econ. Geol. 108, 1523–1540.

Heinrich, C.A., Driesner, T., Stefansson, A., Seward, T.M., 2004. Magmatic vapor contraction and the transport of gold from the porphyry environment to epithermal ore deposits. Geology 32 (9), 761–764.

Hickey, K.A., Ahmed, A.D., Barker, S.L., Leonardson, R., 2014. Fault-controlled lateral fluid flow underneath and into a Carlin-Type Gold deposit: isotopic and geochemical footprints. Econ. Geol. 109, 1431–1460.

Hodges, K., 2003. Geochronology and thermochronology in orogenic systems. In: Heinrich, R., Holland, D., Turekian, K. (Eds.), Treatise on Geochemistry, vols. 3–9. Elsevier Inc., pp. 263–292. https://doi.org/10.1016/B0-08-043751-6/03024-3

Hodgson, C.J., 1989. Patterns of mineralization. In: Bursnall, J.T. (Ed.), Mineralization and Shear Zones, Short Course Notes, 6, pp. 51–88. Montreal.

Hongn, F.D., Del Papa, C., Powell, J., Petrinovic, I., Mon, R., Deraco, V., 2007. Middle Eocene deformation and sedimentation in the Puna-Eastern Cordillera transition (23°-26° S): control by preexisting heterogeneities on the pattern of initial Andean shortening. Geology 35, 271–274.

Kay, S.M., Mpodozis, C., Coira, B., 1999. Neogene magmatism, tectonism and mineral deposits of the Central Andes (22° to 33° S latitude). In: Skinner, B.J. (Ed.), Geology and Ore Deposits of the Central Andes, vol. 7. Society of Economic Geology Special Publication, pp. 27–59.

Lanza, F., Tibaldi, A., Bonali, F.L., Corazzato, C., 2013. Space-time variations of stresses in the Miocene–quaternary along the calama–Olacapato–el Toro fault zone, central Andes. Tectonophysics 593, 33–56.

Leary, S., Sillitoe, R.H., Stewart, P.W., Roa, K.J., Nicolson, B.E., 2016. Discovery, Geology, and Origin of the Fruta del Norte Epithermal Gold-Silver Deposit, Southeastern Ecuador. Econ. Geol. 111, 1043–1072.

Ludwig, K.R., 2003. Isoplot 3.00 A Geochronological Toolkit for Microsoft Excel., 4. Berkeley Geochronology Center, Special Publication.

Mann, P., 2007. Global catalogue, classification and tectonic origins of restraining- and releasing bends on active and ancient strike-slip fault systems. In: Cunningham, W. D., Mann, P. (Eds.), Tectonics of Strike-Slip Restraining and Releasing Bends, vol. 290. Geological Society, London, Special Publications, pp. 13–142.

Marquetti, C., Peroni, J., Seggiaro, R., 2017. Exploración minera con datos satelitales y aeromagnéticos en la región de San Antonio de los Cobres, Puna Oriental. XX Congreso Geológico Argentino. San Miguel de Tucumán.

Marrett, R.A., Allmendinger, R.W., Alonso, R.N., Drake, R.E., 1994. Late Cenozoic tectonic evolution of the Puna Plateau and adjacent foreland, northwestern Argentine Andes. J. S. Am. Earth Sci. 7, 179–207.

Marrett, R, Strecker, M.R., 2000. Response of intracontinental deformation in the central Andes to the late Cenozoic reorganization of South American Plate motions. Tectonics 19, 452–467. https://doi.org/10.1029/1999TC001102.

Matteini, M., Omarini, R.H., Mazzuoli, R., Handler, R., 2002. New Ar/Ar ages for the Tul-Tul, del Medio and Pocitos Volcanic Complex (Puna, Central Andes, 24°S): geodynamic implications. Actas del Congr. Geol. Argent. 1, 117–120. El Calafate.

Micklethwaite, S., 2009. Mechanisms of faulting and permeability enhancement during epithermal mineralisation: cracow goldfield, Australia. J. Struct. Geol. 31, 288–300.

Micklethwaite, S., Sheldon, H.A., Baker, T., 2010. Active fault and shear processes and their implications for mineral deposit formation and discovery. J. Struct. Geol. 32, 151–165.

Montero-López, C., Hongn, F., López-Steinmetz, R., 2017. Geometrías de crecimiento en sedimentos paleógenos en el borde Puna-Cordillera Oriental en la provincia de Jujuy. Congr. Geol. Argent. Tucuman Acta 115–116.

Norini, G., Báez, W., Becchio, R., Viramonte, J., Giordano, G., Arnosio, M., Pinton, A., Groppelli, G., 2013. The Calama-Olacapato-El Toro fault system in the Puna Plateau, Central Andes: geodynamic implications and stratovolcanoes emplacement. Tectonophysics 608, 1280–1297.

Norini, G., Cogliati, S., Báez, W., Arnosio, M., Bustos, E., Viramonte, J., Groppelli, G., 2014. The geological and structural evolution of the Cerro Tuzgle Quaternary stratovolcano in the back-arc region of the Central Andes, Argentina. J. Volcanol. Geoth. Res. 285, 214–228.

Oncken, O., Hindle, D., Kley, J., Elger, K., Victor, P., Schemmann, K., 2006. Deformation of the central Andean upper plate system—facts, fiction, and constraints for plateau models. In: Oncken, O., Chong, G., Frank, G., Giese, P., Ramos, V.A., Strecker, M.R., Wigger, P. (Eds.), The Andes: Active Subduction Orogeny. Springer, pp. 3–27. https://doi.org/10.1007/978-3-540-48684-8_1.

Ortner, H., Reiter, F., Acs, P., 2002. Easy handling of tectonic data: the programs TectonicVB for Mac and TectonicsFP for window. Comput. Geosci. 28, 1193–1200.
Peacock, D.C.P., Anderson, M.W., Rotevatn, A., Sanderson, D.J., Tavarnelli, E., 2017a. The interdisciplinary use of "overpressure. J. Volcanol. Geoth. Res. 341, 1–5.
Peacock, D.C.P., Tavarnelli, E., Anderson, M.W., 2017b. Interplay between stress permutations and overpressure to cause strike-slip faulting during tectonic inversion. Terra. Nova 29, 61–70.
Petit, J., 1987. Criteria for the sense of movement on fault surfaces in brittle rocks. J. Struct. Geol. 9, 597–608.
Petrinovic, I.A., Martí, J., Aguirre-Díaz, G.J., Guzmán, S., Geyer, A., Salado Paz, N., 2010. The Cerro Aguas Calientes caldera, NW Argentina: an example of a tectonically controlled, polygenetic collapse caldera, and its regional significance. J. Volcanol. Geoth. Res. 194, 15–26.
Petrinovic, I.A., Grosse, P., Guzmán, S., Caffe, P., 2017. Evolución del volcanismo Cenozoico en la Puna Argentina. In: Muruaga, C.M., Grosse, P. (Eds.), Ciencias de la Tierra y Recursos Naturales del NOA. Relatorio del XX Congreso Geológico Argentino. San Miguel de Tucumán, pp. 469–483.
Petrinovic, I.A., Hernando, I.R., Guzmán, S.R., 2021. Miocene to Recent collapse calderas of the southern and central volcanic zones of the Andes and their tectonic constraints. Int. J. Earth Sci. 110, 2399–2434.
Quade, J., Dettinger, M.P., Carrapa, B., DeCelles, P., Murray, K.E., Huntington, K.W., Cartwright, A., Canavan, R.R., Gehrels, G., Clementz, M., 2015. The growth of the central Andes, 22°-26° S. In: DeCelles, P.G., Ducea, M.N., Carrapa, B., Kapp, P.A. (Eds.), Geodynamics of a Cordilleran Orogenic System: the Central Andes of Argentina and Northern Chile, vol. 212. Geological Society of America Memoir, pp. 277–308.
Ramelow, J., Riller, U., Romer, R., Oncken, O., 2005. Kinematic link between episodic trap door collapse of the Negra Muerta caldera and motion on the Olacapato-el Toro fault zone, southern central Andes. Int. J. Earth Sci. 95, 529–541.
Ramos, V.A., 2009. Anatomy and global context of the Andes: main geologic features and the Andean orogenic cycle. Backbone Am: Shallow Subduction Plateau Uplift Ridge Terrane Collision 204, 31–65.
Ramos, V.A., 2017. Las provincias geológicas del noroeste argentino. In: Muruaga, C.M., Grosse, P. (Eds.), Ciencias de la Tierra y Recursos Naturales del NOA. Relatorio del XX Congreso Geológico Argentino. San Miguel de Tucumán, pp. 38–52.
Reiter, F., Acs, P., 2000. TectonicsFP 1.6. Computer Software for Structural Geology, Operating Manual, p. 48.
Renne, P.R., Swisher, C., Deino, A.L, A.L., Karner, D.B., D.B., Owens, T., DePaolo, D.J., 1998. Intercalibration of standards, absolute ages and uncertainties in $^{40}Ar/^{39}Ar$ dating. Chem. Geol. 145, 117–152.
Richards, J., Ullrich, T., Kerrich, R., 2006. The Late Miocene-Quaternary Antofalla volcanic complex, southern Puna, NW Argentina: protracted history, diverse petrology, and economic potential. J. Volcanol. Geoth. Res. 152, 197–239.
Riller, U., Oncken, O., 2003. Growth of the central Andean Plateau by tectonic segmentation is controlled by the gradient in crustal shortening. J. Geol. 111, 367–384.
Riller, U., Petrinovic, I., Ramelow, J., Strecker, M., Oncken, O., 2001. Late Cenozoic tectonism, collapse caldera and plateau formation in the central Andes. Earth Planet Sci. Lett. 188, 299–311.
Robert, F., Poulsen, K.H., Cassidy, K.F., Hodgson, C.J., 2005. Gold metallogeny of the superior and Yilgarn cratons. In: Economic Geology 100th Anniversary, ume, pp. 1001–1033.
Robl, K., 2003. Miozäne Ag-Pb Mineralization des El Quevar Stratovulkan Komplex, Salta, Argentinien. Doctoral thesis. University of Salzburg (unpublished), p. 232.
Robl, K., De Brodtkorb, M.K., Ametrano, S., 2009. La mineralización epitermal miocena del Complejo Estratovolcánico Quevar, Salta. Rev. Asoc. Geol. Argent. 64 (3), 525–539.
Ryan, W.B.F., Carbotte, S.M., Coplan, J., O'Hara, S., Melkonian, A., Arko, R., Weissel, R. A., Ferrini, V., Goodwillie, A., Nitsche, F., Bonczkowski, J., Zemsky, R., 2009. Global Multi-Resolution Topography (GMRT) synthesis data set. Geochem. Geophys. Geosyst. 10 (Q03014). doi:10.1029/2008GC002332.
Schreurs, G., 2003. Fault development and interaction in distributed strike-slip shear zones: an experimental approach. In: Storti, F., Holdsworth, R.E., Salvini, F. (Eds.), Intraplate Strike-Slip Deformation Belts, vol. 210. Geological Society, London, Special Publications, pp. 35–52.
Sébrier, M., Mercier, J.L., Macharé, J., Bonnot, D., Cabrera, J., Blanc, J.L., 1988. The state of stress in an overriding plate situated above a flat slab: the Andes of central Perú. Tectonics 7, 895–928.
Seggiaro, R.E., Hongn, F.D., 1999. Influencia tectónica en el volcanismo Cenozoico del Noroeste argentino. Acta Geol. Hisp. 34, 227–242.
Seggiaro, R.E., Guzmán, S., Pereyra, R., Coppolecchia, M., Cegarra, M., 2016. Neotectónica y volcanismo monogenético cuaternario sobre el segmento central del lineamiento Calama Olacapato Toro, NO argentino. Rev. Asoc. Geol. Argent. 73 (4), 468–477.
Seggiaro, R.E., Guzmán, S.R., Apaza, F.D., 2017. Control estructural sobre el magmatismo en los alrededores de San Antonio de Los Cobres, sector oriental de la Puna central. In: Muruaga, C.M., Grosse, P. (Eds.), Ciencias de la Tierra y Recursos Naturales del NOA. Relatorio del XX Congreso Geológico Argentino. San Miguel de Tucumán, pp. 142–146.
Seggiaro, R., Guzman, S., Marti, J., 2019. Dynamics of caldera collapse during the Coranzulí eruption (6.6 Ma) (central Andes, Argentina). J. Volcanol. Geoth. Res. 374, 1–12.
Seggiaro, R.E., Molina, E.A., Heredia Carballo, N., Escuder Viruete, J., Marquetti, C., 2021. Evaluación metalogenética y estudio geológico-estructural del distrito polimetálico de San Antonio de los Cobres, provincias de Salta y Jujuy, República Argentina. In: Parte I: Contexto geológico-estructural regional del Complejo Volcánico El Quevar. Contribuciones Técnicas Recursos Minerales 46, 6-24. ISSN 2618-5032. Informe Final, p. 29. https://repositorio.segemar.gov.ar/handle/30884 9217/4182.
Sibson, R.H., 1990. Conditions for Fault-Valve Behavior, vol. 54. Geological Society, London, Special Publications, pp. 15–28.
Sibson, R.H., 1992. Implications of fault-valve behaviour for rupture nucleation and recurrence. Tectonophysics 211, 283–293.
Sibson, R.H., 2001. Seismogenic framework for hydrothermal transport and ore deposition. Rev. Econ. Geol. 14, 25–50.
Sibson, R.H., 2020. Preparation zones for large crustal earthquakes consequent on fault-valve action. Earth Planets Space 72, 31.
Sillitoe, R.H., 2010. Porphyry copper systems. Econ. Geol. 105 (1), 3–41.
Sillitoe, R.H., 2015. Epithermal paleosurfaces. Miner. Deposita 50, 767–793.
Simmons, S.F., White, N.C., John, D.A., 2005. Geological characteristics of epithermal precious and base metal deposits. In: Economic Geology 100th Anniversary, ume, pp. 485–522.
Sperner, B., Zweigel, P., 2010. A plea for more caution in fault-slip analysis. Tectonophysics 482 (1–4), 29–41.
Sulpizio, R., Massaro, S., 2017. Influence of stress field changes on eruption initiation and dynamics: a review. Front. Earth Sci. 5, 18.
Tibaldi, A., Bonali, F., Corazzato, C., 2017. Structural control on volcanoes and magma paths from local to orogeny-scale: the Central Andes case. Tectonophysics 699, 14–41.
Trumbull, R., Riller, U., Oncken, O., Scheuber, E., Munier, K., Hongn, F., 2006. The time-space distribution of Cenozoic arc volcanism in the Central Andes: a new data compilation and some tectonic considerations. In: Oncken, O., Chong, G., Franz, G., Giese, P., Götze, H.J., Ramos, V., Strecker, M., Wigger, P. (Eds.), The Andes - Active Subduction Orogeny. Springer-Verlag, Berlin, pp. 29–43.
Twiss, R.J., Unruh, J.R., 1998. Analysis of fault slip inversions: do they constrain stress or strain rate? J. Geophys. Res. 103 (6), 12–205. –12.222.
Woodcock, N.H., Fisher, M., 1986. Strike-slip duplexes. J. Struct. Geol. 8 (7), 725–735.
Wiemer, D., Steffen, G., Hagemann, N., Thébaud, C., 2021. Role of Basement Structural Inheritance and Strike-Slip Fault Dynamics in the Formation of the Pataz Gold Vein System, Eastern Andean Cordillera, Northern Peru. Econ. Geol. 116 (7), 1503–1535. https://doi.org/10.5382/econgeo.4839.
Woodcock, N.H., Dickson, J.A.D., Tarasewicz, J.P.T., 2007. Transient permeability and reseal hardening in fault zones: evidence from dilation breccia textures. In: Geological Society, 270. Special Publications, London, pp. 43–53.
Yamaji, A., Sato, K., 2011. Clustering of fracture orientations using a mixed Bingham distribution and its application to paleostress analysis from dike or vein orientations. J. Struct. Geol. 33, 1148–1157.
Yamaji, A., Sato, K., Tonai, S., 2010. Stochastic modeling for the stress inversión of vein orientations: paleostress analysis of Pliocene epithermal veins in southwestern Kyushu, Japan. J. Struct. Geol. 32, 1137–1146.